M 2025

U.PORTO
FEUP FACULDADE DE ENGENHARIA
UNIVERSIDADE DO PORTO

PARAMETRIC STUDIES OF NON-ISOTHERMAL REACTORS USING CFD

LUÍS MIGUEL KLUT SOARES
MASTER'S THESIS IN CHEMICAL ENGINEERING
PRESENTED TO THE FACULTY OF ENGINEERING
OF THE UNIVERSITY OF PORTO

Master in Chemical Engineering

Parametric studies of non-isothermal reactors using CFD

Master's Thesis

of

Luís Miguel Klut Soares

Developed within the scope of the Dissertation course unit

held in

Associate Laboratory in Chemical Engineering

ALiCE ASSOCIATE LABORATORY IN CHEMICAL ENGINEERING

Supervisor at FEUP: **Prof. José Daniel Araújo**
Co-supervisor at FEUP: **Prof. Luís Miguel Madeira**

U.PORTO
FEUP FACULDADE DE ENGENHARIA UNIVERSIDADE DO PORTO
DEPARTAMENTO DE ENGENHARIA QUÍMICA E BIOLÓGICA

November 17, 2025

Acknowledgements

First, I would like to deeply thank my parents for allowing me the opportunity of attending this course and for the unconditional support they have given me, alongside my closest friends.

Secondly, I would like to thank my supervisors, Professor José Araújo and Professor Luís Madeira, who guided me throughout this work, providing insights, ideas and their time for discussion and corrections.

Dr. José Daniel Araújo, supervisor of this dissertation, is an integrated member of CEFT – Transport Phenomena Research Center, supported by national funds through FCT/MCTES (PIDDAC): LA/P/0045/2020 (ALiCE), UIDB/00532/2020 and UIDP/00532/2020 (CEFT).

Prof. Luís Miguel Madeira, co-supervisor of this dissertation, is an integrated member of LEPABE – Laboratory for Process Engineering, Environment, Biotechnology and Energy, supported by national funds through FCT/MCTES (PIDDAC): LEPABE, UIDB/00511/2020 (DOI: 10.54499/UIDB/00511/2020) and UIDP/00511/2020 (DOI: 10.54499/UIDP/00511/2020) and ALiCE, LA/P/0045/2020 (DOI: 10.54499/LA/P/0045/2020).

Resumo

Este trabalho apresenta um estudo paramétrico sistemático de um reator não-isotérmico com CFD através do pacote de software ANSYS *Workbench*® 2025 R1, com o intuito de avaliar o efeito que condições de entrada e de operação têm na composição e temperaturas médias na saída. O domínio e a malha foram criadas no *DesignModeler*® e *Meshing*®, respetivamente, e um teste de independência de malha for executado para selecionar um tamanho de elemento de malha adequado para o estudo paramétrico. Depois, com o objetivo de obter uma perspetiva sobre a hidrodinâmica do sistema, simulações transientes foram feitas para replicar experiências de *tracer*, com uma perturbação em degrau. Como ponto principal desta tese, simulações automáticas em estado estacionário foram executadas com uma reação hipotética, exotermal e homogénea, $A + B \rightarrow 2C$, numa gama de condições. A influência dos seguintes parâmetros chave foi avaliada: a velocidade da entrada; temperatura da entrada; composição molar da entrada (da espécie A, B, e uma espécie inerte adicional, para diluição); coeficiente de transferência de calor convectivo e temperatura do meio exterior; e parâmetros da reação (k_0, E_a, ΔH).

As simulações de *tracer* permitiram a previsão da distribuição dos tempos de residência (RTD) e o valor do tempo de residência médio, que indica a presença de caminhos preferenciais, visto que os valores obtidos de $\overline{t_r}$ foram sempre mais elevados do que τ.

Uma transição de regime turbulento para laminar foi observada com a diminuição da velocidade de entrada, reduzindo mistura e a conversão obtida, apesar do tempo de residência mais elevado. Para valores de Reynolds (entre 500 e 1000) com mistura suficiente, o *feedback* positivo entre temperatura e a reação resulta em *runaway* térmico; em contraste, casos laminares com mistura limitada evitam *runaway* com níveis de conversão baixa. Adicionar arrefecimento externo reduziu temperaturas perto da parede do reator mas não afetou os pontos mais quentes do reator no interior, sendo insuficiente para remover todo o calor libertado pela reação. Isto demonstra a necessidade de elementos de arrefecimento internos para controlar a temperatura das zonas internas. Diluição da entrada foi testada em duas configurações: estequiómetricamente, ao reduzir a composição de entrada da espécie A e B igualmente; e com o reagente A em excesso, diminuindo a composição de B. Esta diluição foi eficaz em limitar a energia térmica total libertada, mantendo níveis de conversão alta, nos casos com A em excesso. Diminuir a entalpia da reação resulta num sistema mais sensível, com *runaway* a acontecer mais vezes.

Do grande número de simulações feitas neste estudo paramétrico, o sistema com os valores de temperatura mais realistas com uma conversão apreciável utilizou os seguintes parâmetros e condições fronteira: $k_0 = 500\, m^3 \cdot kmol^{-1} s^{-1}$, $E_a = 35\, kJ \cdot mol^{-1}$, $\Delta H = -50\, kJ \cdot mol^{-1}$, $T_{inlet} = 320\, K$, $T_{outside} = 300\, K$, $h = 1000\, W \cdot m^{-2} s^{-1}$.

O trabalho conclui com uma avaliação da metodologia utilizada, que permitiu a criação quase automática da grande quantidade de resultados, apesar de ter algumas limitações, e propostas para trabalho futuro, particularmente no estudo e validação de modelos de turbulência e no uso dos dados produzidos na exploração futura de reações exotérmicas.

Palavras-chave: CFD, estudo paramétrico, reação exotérmica

Abstract

This work presents a systematic parametric study of a non-isothermal reactor using CFD in the ANSYS Workbench® 2025 R1 suite, with the aim of evaluating the effect of inlet conditions and operating parameters on the average composition and temperature at the outlet. The domain and mesh were created in DesignModeler® and Meshing®, respectively, and a mesh independence test was performed to select an adequate mesh element size for the parametric study. Afterwards, with the goal of getting an overview of the hydrodynamic behaviour of the system, transient simulations were made to replicate tracer experiments, with a step input. As the central part of this thesis, automated steady state simulations were carried out including a hypothetical homogeneous exothermic reaction, $A + B \rightarrow 2C$, under a wide range of conditions. The influence of key parameters was inspected, which comprised of: inlet velocity; inlet temperature; inlet reactant molar fractions (of species A, B and an additional inert species, for inlet dilution); external convective heat transfer coefficient and outside medium temperature; and reaction parameters (k_0, E_a, ΔH).

Tracer simulations allowed prediction of residence time distributions (RTD) and mean residence times, indicating the presence of preferential paths due to $\overline{t_r}$ values greater than the calculated τ.

A transition from turbulent to laminar regimes was observed as inlet velocity decreased, producing poorer mixing and lower production despite longer residence times. For inlet Reynolds values (between 500 and 1000) with sufficient mixing, the feedback loop between temperature and reaction rate produced thermal runaways; by contrast, laminar cases with limited mixing avoided runaway but suffered low conversion. Adding external cooling reduced near-wall temperatures but left inner reactor hotspots largely unaffected, being insufficient to remove the heat released by the reaction. This shows the need for internal cooling elements to provide cooling to the hottest regions. Inlet dilution was tested in two arrangements: stoichiometrically, reducing the feed of species A and B equally; and in configurations with species A in excess and a reduced feed of B. This proved to be effective at limiting total heat energy release while maintaining conversion levels using an excess of species A. Reducing reaction enthalpy increased the occurence of thermal runaway.

From the large set of simulations involved in this parametric work, the system with the most reasonable temperature levels while maintaining an appreciable conversion of 45% used the following parameters and boundary conditions: $k_0 = 500\, m^3 \cdot kmol^{-1} s^{-1}$, $E_a = 35\, kJ \cdot mol^{-1}$, $\Delta H = -50\, kJ \cdot mol^{-1}$, $T_{inlet} = 320\, K$, $T_{outside} = 300\, K$, $h = 1000\, W \cdot m^{-2} s^{-1}$.

The work concludes with an evaluation of the used methodology, which allowed for the almost automatic creation of the large amount of results presented in this study, although with some limitations, and future prospects following this thesis, particularly in the exploration and validation of turbulence models and the use of the produced dataset in further exploration of exothermic reactions.

Keywords: CFD, parametric study, exothermic reaction.

Declaration

I hereby declare, under word of honour, that this work is original and that all non-original contributions are indicated and due reference is given to the author and source.

Luís Miguel Klut Soares
Porto, 28th of September of 2025

Index

List of figures

List of tables

Notation and Glossary

Co	Courant number	
C	Concentration	mol·m^3
C_p	Specific heat capacity	J·kg^{-1}·K^{-1}
D	Diameter	m
e	Internal energy	J
E	Total energy	J
E_a	Activation energy	J·mol^{-1}
$\vec{F}$	External forces	N
$\vec{g}$	Gravitational force	N
h	Convective heat transfer coefficient	W·m^{-2}·K^{-1}
H	Total enthalpy	J
$\vec{J}$	Diffusion flux	mol·m^{-2}·s^{-1}
k	Kinetic constant	m^3·mol^{-1}·s^{-1}
k_0	Pre-exponential factor	m^3·mol^{-1}·s^{-1}
k_c	Thermal conductivity	W·m^{-1}·K^{-1}
k_e	Turbulent kinetic energy	m^2·s^{-2}
L	Length	m
p	Static pressure	Pa
Q	Flow rate	m^3·s^{-1}
R	Rate of production through chemical reaction	mol·s^{-1}
Re	Reynolds number	
R_g	Ideal gas constant	J·mol^{-1}·K^{-1}
S	Source term	
t	Time	s
T	Temperature	K
$\overline{t_r}$	Mean residence time	s
U	Flow velocity	m·s^{-1}
V	Volume	m^3
$\vec{v}$	Velocity vector	m·s^{-1}
x	Molar fraction	

Greek Letters

Δh	Mesh element size	m
ΔH	Reaction enthalpy	$J \cdot mol^{-1}$
Δt	Time variation	s
ε	Turbulent dissipation rate	$m^2 \cdot s^{-3}$
$\vec{\tau}$	Stress tensor	Pa
μ	Viscosity	$Pa \cdot s^{-1}$
ρ	Density	$kg \cdot m^{-3}$
τ	Space-time	s

Indexes

i	Species

Functions

F(t)	Dankwerts F curve	
E(t)	Residence time distribution	s^{-1}

List of Acronyms

CFD	Computational Fluid Dynamics
CAD	Computer-Aided Design
DNS	Direct Numerical Simulation
RTD	Residence Time Distribution
RANS	Reynolds-Averaged Navier-Stokes
SDG	Sustainable Development Goals
SRS	Scale Resolving Simulation
TUI	Text User Interface

1. Introduction

1.1. Project framing and presentation

Industry 4.0, the fourth industrial revolution, refers to the digital transformation of manufacturing and engineering through the use of data-driven methods. Using advancements such as the Internet of Things, databases, computer networks, and gathered datasets from physical processes, relevant features from products and processes can be predicted. These approaches enable optimisation and rapid prototyping via digital methods [1], facilitating the scale up and reliability of testing procedures over a wide range of operating conditions [2].

Regarding the simulation of complex multiphysics phenomena typical of Chemical Engineering, Computational Fluid Dynamics (CFD) tools have seen their use expanded due to the rise of available computing power over the course of the 21st century, becoming not only a tool for process analysis but also for optimisation and prototyping, as calculation time is gradually reduced and CFD tools become more widespread and available. Furthermore, the increasingly wider range of high-quality datasets on the internet or directly obtained from physical processes has led to the development of more reliable and accurate models to describe relevant features of phenomena such as heat and mass transfer, as well as chemical reaction, for varied operating conditions [3], propelling the uses of CFD even further.

In the design process, CFD is highly relevant to produce parametric studies without the need for dedicated experimental setups and tests, simplifying the scale up process while providing easy methods of visualising traditionally complex phenomena, such as flow fields. These uses of CFD can also be leveraged in the analysis of already existing processes, using measured data from sensors.

From a plant scale perspective, CFD presents some interesting possibilities, allowing for on-the-spot simulation using input data measured directly from the plant, which could aid in process control. However, the time requirements needed for accurate CFD predictions rules out the direct use of CFD in this situation [4].

To circumvent this issue, CFD can be used to develop tailored, high-quality datasets of the response of specific units to changes in operating conditions. These datasets can then be used to train machine learning models that approximate the response in a fraction of the time that would be needed while using CFD [2, 4].

In this context, this project seeks to carry out a parametric study of a non-isothermal reactor, taking advantage of the capabilities of the ANSYS commercial software package to produce a compilation of numerical data to evaluate the effect of individual parameters on reactor performance, while using data visualisation to identify potential improvements and limitations, following interpretation of the obtained results.

1.2. Author contributions to the project

All simulations and their associated results were carried out and obtained by the author, alongside the calculation and determination of all parameters used. Organisation and presentation of data obtained from plot creation to contour creation was performed by the author. Interpretation and discussion of the obtained results was done by the author, with guidance from the project supervisors.

1.3. Thesis Organization

This work is structured as follows. The state of the art (chapter 2) is divided into three parts: first, an introduction to the application of CFD tools and the governing equations underlying the numerical algorithms used for predictions; second, an overview of turbulence modelling strategies, with emphasis on the k-ε family of models, due to their relevance in this study; third, a review of two representative studies to highlight the relevance of CFD in chemical engineering, demonstrating how CFD can be used to predict reactor behaviour, test hypothesis and enable data visualisation.

The following chapter (chapter 3) outlines the methodology and workflow defined for this work, stepping through the stages required to perform a parametric study: geometry and domain creation, mesh generation and independence testing, tracer predictions, and the parametric study itself.

The results and discussion (chapter 4) presents the obtained results in the order of the defined methodology. It begins with the mesh independence to determine the mesh element size, followed by analysis of residence time distribution (RTD) curves. The main results from the parametric study are then discussed, with each subsection focusing on the effects of the variation of a inlet or operation parameter.

The conclusions section (chapter 5) summarizes the main findings and provides suggestions for future work.

In the Assessment of the work performed section (chapter 6), the achieved goals are evaluated and SDGs that this work contributes to are presented. This section finishes with a personal perspective with regards to the work.

Annex A presents the symbols of the SDGs that this work contributes to.

Lastly, the appendices contain supplementary material: Appendix A lists the dimensions of the geometries used throughout this work, while Appendix B presents the results obtained in a preliminary parametric study that produced unrealistic cases regarding the temperature levels observed, included due to the effort and time expenditure used in its creation and its produced data.

2. State of the Art

In recent years, CFD has emerged as a powerful tool to capture fluid flow, heat transfer and reaction behaviour in complex geometries, allowing systematic exploration of operating and design parameters without the need for potentially costly experimental installations or simplified assumptions [5]. CFD can be understood as being built upon three key pillars: Fluid Mechanics; Computer Science and Mathematics. It applies numerical methods and computing power to model the behaviour of systems involving fluid flow by solving the governing fundamental equations of conservation of mass, momentum and energy, presented in subchapter 2.1.

First, a domain is defined, generally created using Computer-Aided Design (CAD) tools to represent the desired geometry. However, this continuous domain cannot be used directly, as the governing equations are partial differential equations which require numerical methods to solve. As such, the domain is discretized spatially, divided into elements that together form a mesh.

At this point, a solver can be used to calculate the solution variables through the corresponding governing equation, iteratively over the mesh elements. The Pressure-Based Coupled Algorithm, available in ANSYS Fluent® and used throughout this study is shown in figure 2-1. At the end of each iteration, convergence is evaluated using the equation residuals, typically evaluated against a threshold of 10^{-5} or lower, depending on the desired precision [6].

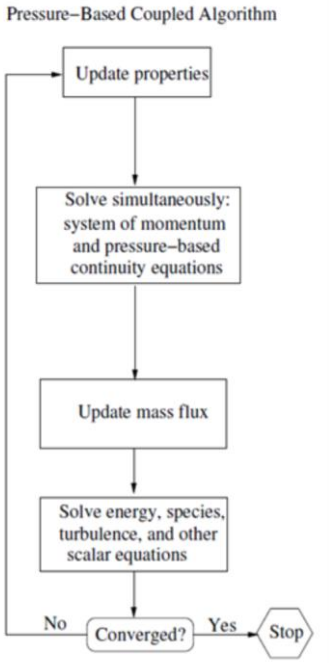

Figure 2-1: Pressure-Based Coupled algorithm used in ANSYS Fluent®, adapted from [6].

2.1. Governing Equations

As mentioned, the core equations of CFD are the conservation laws. The continuity equation, the law of mass conservation applied to the fluid domain, ensures the total mass in the fluid system is kept constant. It is written in a generalized form, suitable for incompressible and compressible flow as Eq. 2-1, although it can be simplified for use in incompressible flows [7].

$$\frac{\partial \rho}{\partial t} + \nabla \cdot (\rho \vec{v}) = 0 \tag{2-1}$$

In this equation, ρ is the fluid density, t is time and $\vec{v}$ is the velocity vector. The addition of a source term, S_m, replacing the right-hand side of the equation can be used to represent mass added from a second phase, such as the condensation of water vapor adding mass to the liquid phase, or other sources [6].

The equation of motion, represented by the Navier-Stokes equations, is the conservation of momentum in the fluid domain, where variations in momentum of fluid elements come from internal and external forces acting upon it [7]. For a Newtonian viscous fluid, the equation is written as Eq. 2-2:

$$\frac{\partial \rho \vec{v}}{\partial t} + \nabla \cdot (\rho \vec{v} \vec{v}) = -\nabla p + \nabla \cdot (\overline{\tau}) + \rho \vec{g} + \vec{F} \tag{2-2}$$

where p is the static pressure, $\overline{\tau}$ is the stress tensor, $\rho \vec{g}$ and $\vec{F}$ are the gravitational and external forces applied on the fluid, respectively.

The energy equation is obtained from the first law of thermodynamics when applied to a fluid element [7], written as follows:

$$\frac{\partial \rho E}{\partial t} + \nabla \cdot (\rho \vec{v} H - k_c \nabla T - \overline{\tau} \cdot \vec{v}) = S_h \tag{2-3}$$

where T is the temperature, S_h is a source term that includes heat generation from chemical reactions and work done on the system, and k_c is the thermal conductivity. In the case of turbulent flow, k_c is the sum of the fluid's thermal conductivity and an additional turbulent thermal conductivity defined in accordance with the turbulence model in use, to obtain the effective thermal conductivity of the fluid [6, 7]. In this equation, E is the total energy of the element by mass, defined by Eq. 2-4:

$$E = e + \frac{\overrightarrow{v^2}}{2} \tag{2-4}$$

where e is the internal energy of the element [7].

H is the total enthalpy of the system and is written as Eq. 2-5.

$$H = E + \frac{p}{\rho} \tag{2-5}$$

The species transport equations predict the variation of each species at a given fluid element, written as Eq. 2-6:

$$\frac{\partial \rho_{mix} Y_i}{\partial t} + \nabla \cdot (\rho \vec{v} Y_i) = -\nabla \cdot \vec{J_i} + R_i + S_i \quad (2\text{-}6)$$

where ρ_{mix} is the density of the mixture, Y_i is the mass fraction of species i, $\vec{J_i}$ is the diffusion flux of species i, R_i is the rate of production of species i through chemical reactions and S_i is the addition of species i through a second phase or other sources [6]. This equation is solved for $n-1$ species, *n* being the total number of species in the system, as the last fraction of the final component can simply be obtained from the fact that mass fractions sum to one.

2.2. Turbulence modeling

Many flows of interest in chemical engineering are turbulent. Turbulence is the unsteady random motion in fluids at high Reynolds numbers, and several features are affected by turbulence, such as flow hydrodynamics, heat transfer and species transport. Turbulent flows can be described solely by the Navier-Stokes equations, and all turbulence scales could be solved directly through these equations using Direct Numerical Simulation (DNS). However, due to the necessary small space and time scales/elements involved, the computational power required is normally prohibitive. Instead, the Navier-Stokes equations are averaged, with one common approach being the Reynolds-Averaged Navier-Stokes (RANS) [8].

In the RANS equations, the flow variables are divided into mean and fluctuating parts, and averaged over time, removing the turbulent structures and providing a smooth variation of the averaged velocity and pressure fields. However, by averaging the Navier-Stokes equations, new terms are added to the transport equations, the Reynolds stresses and fluxes [8]. These terms require suitable turbulence models for calculation, of which there are several options, each one adequate to different situations.

As an alternative to DNS and the RANS equations, Scale-Resolving Simulation (SRS) models are a mix of both, solving a portion of the turbulent spectrum without the averaging used in RANS, at the cost of increased computational cost. This method also depends on small time step sizes and accurate treatment of near wall regions [3, 5].

One of the most frequently used models in industry is the standard k-ε model, a two-equation model that is used due to its robustness and accuracy over a large range of turbulent flows in industrial applications. Nowadays, variations of the original model, such as the RNG and Realizable k-ε models [8], have been created to improve its performance, increasing the range of suitable flows that can be modelled.

The Realizable k-ε model, used in this study to model turbulent flows, obtains the titular k_e, the turbulent kinetic energy, and ε, the dissipation rate, via equations 2-7 and 2-8, respectively [6].

$$\frac{\partial}{\partial t}(\rho k) + \frac{\partial}{\partial x_i}(\rho k u_i) = \frac{\partial}{\partial x_i}\left[\left(\mu + \frac{\mu_t}{\sigma_k}\right)\frac{\partial k}{\partial x_i}\right] + G_k + G_b - \rho\varepsilon - Y_m + S_k \quad (2\text{-}7)$$

$$\frac{\partial}{\partial t}(\rho \varepsilon) + \frac{\partial}{\partial x_i}(\rho \varepsilon u_i) = \frac{\partial}{\partial x_i}\left[\left(\mu + \frac{\mu_t}{\sigma_k}\right)\frac{\partial \varepsilon}{\partial x_i}\right] + \rho C_1 S\varepsilon - \rho C_2 \frac{\varepsilon^2}{k+\sqrt{(v\varepsilon)}} + C_{1\varepsilon}\frac{\varepsilon}{k_e}C_{3\varepsilon}G_b + S_\varepsilon \quad (2\text{-}8)$$

Herein, G_k represents the generation of turbulent kinetic energy due to the mean velocity gradients. G_b is the generation of turbulence kinetic energy due to buoyancy. Y_m represents the contribution of the fluctuating dilatation in compressible turbulence to the overall dissipation rate. C_2 and $C_{1\varepsilon}$ are constants, σ_k and σ_ε are the turbulent Prandtl numbers for k and ε, respectively, and S_k and S_ε are user-defined source terms. The constants and turbulent Prandtl numbers are model constants, widely accepted and used in Fluent® as $C_{1\varepsilon} = 1.44$, $C_2 = 1.9$, $\sigma_k = 1.0$ and $\sigma_\varepsilon = 1.2$ [6].

2.3. Relevance of CFD in Chemical Engineering

In chemical engineering, CFD is a powerful tool for understanding and designing complex processes and simultaneous phenomena. More specifically in reaction engineering, CFD allows the description of chemical reaction kinetics, multiphase flows, residence time distribution (RTD) prediction, temperature distributions, among many other applications, providing key insight into features that are difficult to observe and/or detail experimentally [8].

Two different studies were selected to show the use of CFD in reactor design and optimisation, showcasing the visualisation of key reactor features in simple to understand images and the parametric testing of operating conditions and parameters that CFD allows. Moon *et al.* [9] developed a multi-tubular reactor for butadiene synthesis using OpenFOAM, an open-source CFD system, shown in figure 2-2.

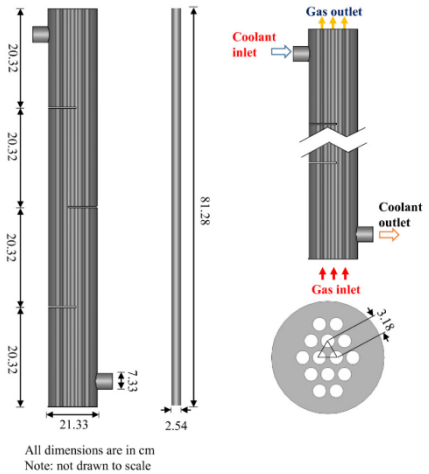

Figure 2-2: Developed reactor for butadiene synthesis, adapted from [9].

Following the initial created design, a parametric study was performed by varying the inlet temperature and velocity, as well as reactor thermal conditions, switching operation between adiabatic, non-isothermal and isothermal. The effects of these parameters were evaluated by comparing the conversion, selectivity and yield of the butadiene synthesis, validating the obtained results with experimental installations from previous works.
The simulations were able to clearly demonstrate the differences between the different test cases, showing the effect of the different operating conditions, as summarized in table 2-1.

Table 2-1: Yield of 1,3-butadiene obtained for each thermal condition, adapted from [9].

Thermal Condition	Yield (%)
Isothermal	24.35%
Non-isothermal	88.38%
Adiabatic	92.81%

As the thermal conditions change overall yield increases due to higher internal reactor temperatures, peaking in the adiabatic case due to higher temperatures, as seen on figure 2-3. Mole fraction profiles averaged over each tube, figure 2-4, indicate the gradual conversion of the reagents until these are fully consumed, corresponding to the plateaus in both mole fraction and temperature, for the adiabatic case.

This study clearly illustrates one of the strengths of CFD, the visualisation of reactor variables and the effect of operating conditions without the need for physical tests and installations.

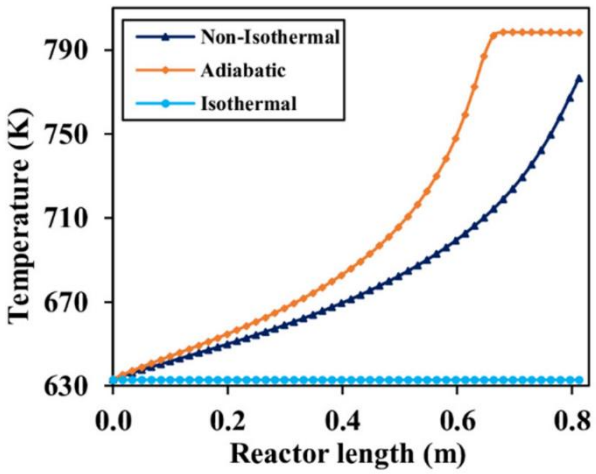

Figure 2-3: Temperature profiles for each thermal condition, adapted from [9].

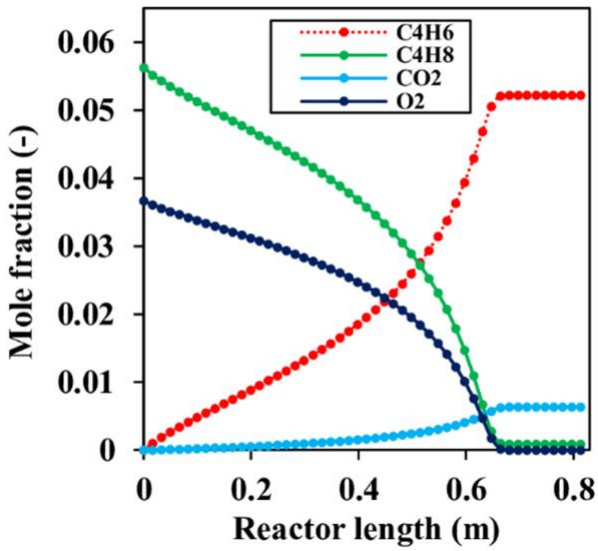

Figure 2-4: Mole fraction profiles for the adiabatic case, adapted from [9].

Soto *et al.* [5] conducted a similar study, designing a multi-tubular reactor to produce substitute natural gas (SNG) from carbon dioxide (CO_2) via methanation. In this work, Fluent® was used.

One of the goals of the study was to perform an in-depth analysis of the coolant system, due to the presence of temperature hotspots both in the internal pipes and in the shell, which was something that had been underestimated by assumptions in previous studies. Based on proper mathematical domains, it was shown that CFD can be used to describe and evaluate both reactor side phenomena and shell side fluid flow and heat transfer under industrially relevant conditions. The reactor design is shown in figure 2-5.

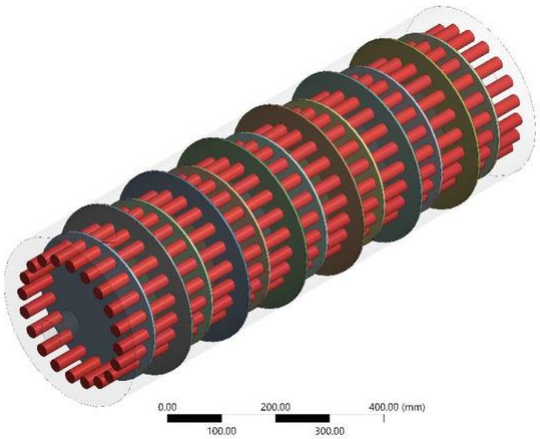

Figure 2-5: Reactor design for SNG production, adapted from [5].

Another strength of CFD is demonstrated in this study, the ability to rapidly evaluate different options to optimise a process.

Two types of coolant were tested, molten salt and thermal oil, at increasing flow rates. The obtained results are summarized in table 2-2. For all flow rates, the molten salt maintains a higher heat transfer coefficient than the thermal oil, resulting in lower temperatures, both maximum and average, although these remain close for all cases. More importantly, as

coolant flow rate increases the difference between the two fluids heat transfer coefficient decreases, with the initial higher performance of the molten salt gradually decreasing and approaching the thermal oil.

From these results, the thermal oil was chosen as the coolant to be used for any further studies, due to not only the similar performance between the fluids, but also because the molten salt coolant requires increased pumping power in comparison to the oil.

Table 2-2: Simulation results for coolant types and flow rate, adapted from [5].

Coolant Flow and Type	Max Temperature (K)	Tube Average Temperature (K)	Coolant Average Temperature (K)	CO_2 Conversion (%)	Average Heat Transfer Coefficient ($W/m^2 K$)
Molten salt	890.9	590.9	528.3	93.0	104
Thermal oil (1 m^3/h)	896.3	616.1	541.2	94.0	57
Molten salt	885.6	566.7	525.5	91.2	235
Thermal oil (3.5 m^3/h)	885.2	571.5	526.9	91.7	184
Molten salt	880.8	561.5	524.3	90.2	413
Thermal oil (7 m^3/h)	880.7	563.4	525.1	90.6	338
Molten salt	880.1	558.3	523.7	89.4	760
Thermal oil (14 m^3/h)	879.5	558.9	524.1	89.4	645

In addition to the performed coolant study, coolant flow is easily visualised in figure 2-6, further showing the ease of data visualization allowed by CFD. The three-dimensional flow field was cut in reactor cross-sections to identify important zones: 1, crossflow; 2, vortex formation; 3, stagnant zones; 4, parallel flow. The regular flow pattern also indicates that all tubes experience similar conditions, throughout their entire length.

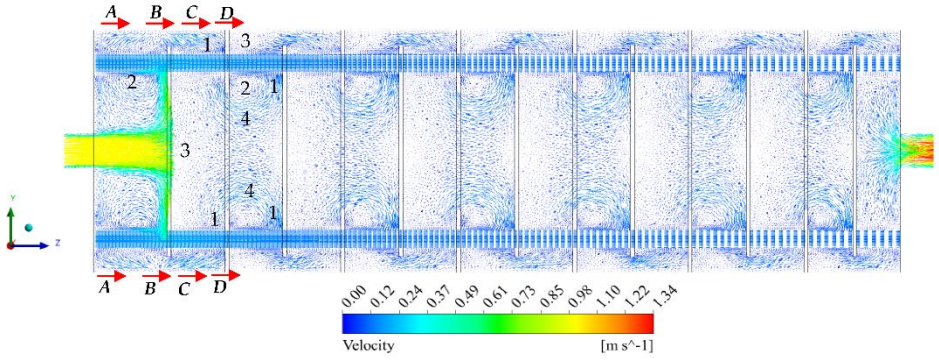

Figure 2-6: Cross-section of coolant velocity field, adapted from [5].

Combining this wealth of data with other simulation techniques at a plant-wide scale allows for extra detail at unit and overall process level. From a top-down approach, plant-wide simulations can be used to design a suitable process, while unit scale simulations using CFD can be used to validate operating conditions, to study the consequences of deviation from the specified parameters to develop suitable safety features [4, 10], to validate used assumptions and to optimize parameters [5].

From the other side, a bottom-up approach, CFD is used in scaling up from kinetic studies and molecular simulations without the need for potentially expensive pilot projects, saving both resources and time [10].

Furthermore, and in accordance with Industry 4.0, simulation software can be used to adapt process controls from incoming real-time plant data, although this requires fast simulation models which might be unsuitable for the specific units. This is especially true for transient CFD simulations that might require hours to complete, especially for complex geometries.

To circumvent this issue, CFD simulations can be performed for a wide range of operating conditions and parameters (in a parametric study), using this information to develop fitting models and applying Machine Learning algorithms that can be used as input to the overall plant model without the need for on-the-spot CFD simulation. One other benefit is the ease of process visualisation to assist operators and designers, such as images of process variables fields, videos and 3D models obtained from post-processing of CFD numerical results. These resources can be used to promote understanding of features of operating units that would otherwise be difficult to observe, such as internal fluid flows and temperature profiles [4].

3. Methodology and Workflow

The present work was conducted with the help of the commercial software platform developed by ANSYS, specifically, the ANSYS Workbench 2025 R1 suite. This platform includes four key programs used throughout the work: DesignModeler®, Meshing®, Fluent®, all integrated within the Workbench® environment. DesignModeler® was used to create the base CAD geometry, which was then processed in Meshing® to generate a simulation-ready mesh, a spatially discretized geometry divided into mesh elements of varying size and shape. Fluent® performs the fluid dynamics simulations, using the mesh and different models for solving the equations of flow, energy and species. Workbench® provides an overarching platform to connect all the other programs, allowing the creation of a centralized workflow that does not necessitate manual tracking of files, and enables parameter-driven updates across the created workflow using design points. Design points are organised into a parameter table in Workbench, where each represents a series of input parameters used in Fluent® (namely boundary conditions), such as inlet flow velocity or inlet temperature, and contain output variables, defined in Fluent®.

3.1. Domain and Mesh Independence

The first step was the creation of the base reactor geometry, made in DesignModeler® and shown in figure 3-1, with dimensions available in Appendix A. The design followed some guiding principles: first, the geometry should remain simple to avoid excessive simulation times; second, it should be suitable for 3D printing to facilitate potential experimental tracer tests, to compare to simulated ones; and third, it should include internal obstacles to introduce flow complexity and promote mixing.

Figure 3-1: Reactor CAD geometry.

Once the reactor geometry was finalised, it was divided into small elements – mesh generation. The size of mesh elements, Δh, significantly influences the quality of the simulation results and must be carefully selected, as it is the spatial discretisation (as can be seen in figure 3-2 for a small portion of the domain) that will be used over the course of the current numerical study; on the other hand, too small Δh implies higher computational times. To determine the optimal size, a mesh independence test should be performed. This involves assigning an initial element size, performing a fluid flow simulation in Fluent®, and recording the average outlet velocity and outlet velocity profile to assess the mesh independence of these results.

The mesh is refined iteratively by dividing element size in half until the difference in average outlet velocity and outlet velocity profiles is sufficiently reduced. At this point, further refinement would not provide additional accuracy, establishing the final mesh element size. As the inlet flow velocity was one of the study parameters, mesh independence was tested at the maximum velocity planned for the parametric study.

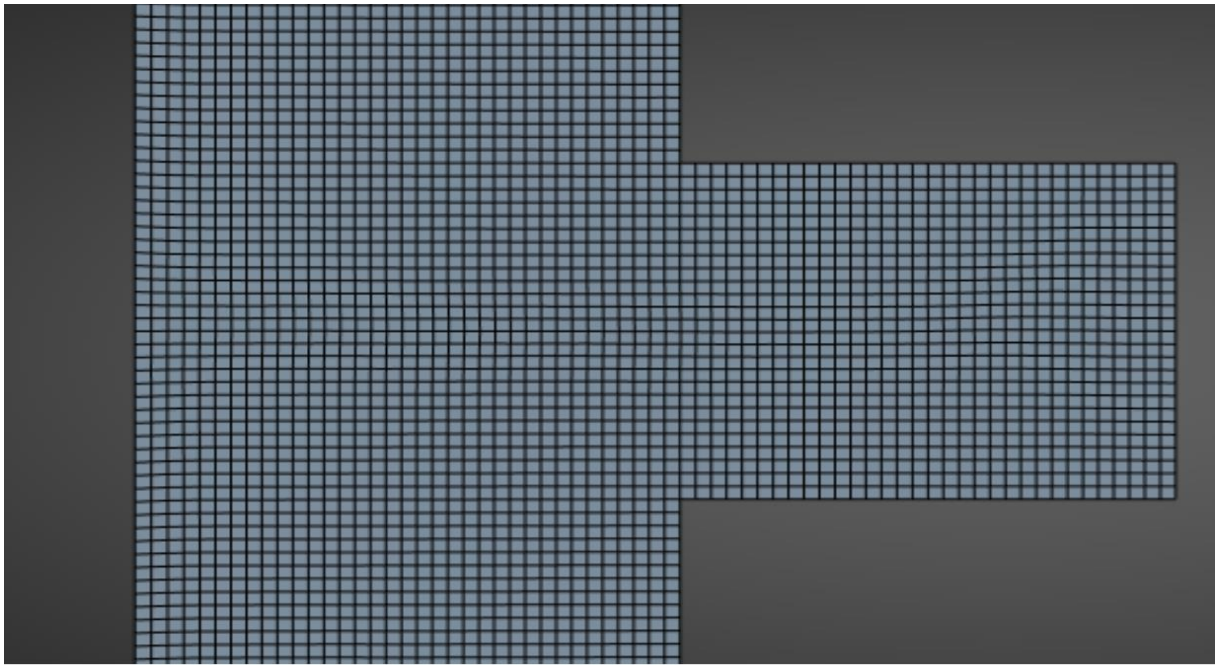

Figure 3-2: Close up of mesh elements at the reactor outlet.

Another important part of mesh creation is the assignment of named selections, which are used in Fluent® to define boundary conditions. As is seen in figure 3-3, the following named selections were created to define the boundary conditions: the edges that represent the inlets, D and E; the outlet, F; and the inner and outer walls, B and C respectively. By naming these selections as inlet, outlet and walls, Fluent® automatically identifies the type of boundary conditions that should be applied. As an example, Fluent® defines the inlet named selection as an edge from where fluid can enter the mesh, setting everything up so that the user only has to change the values to what is required.

Of course, although Fluent® does this automatically, boundary condition type can be directly changed by the user and frequently are.

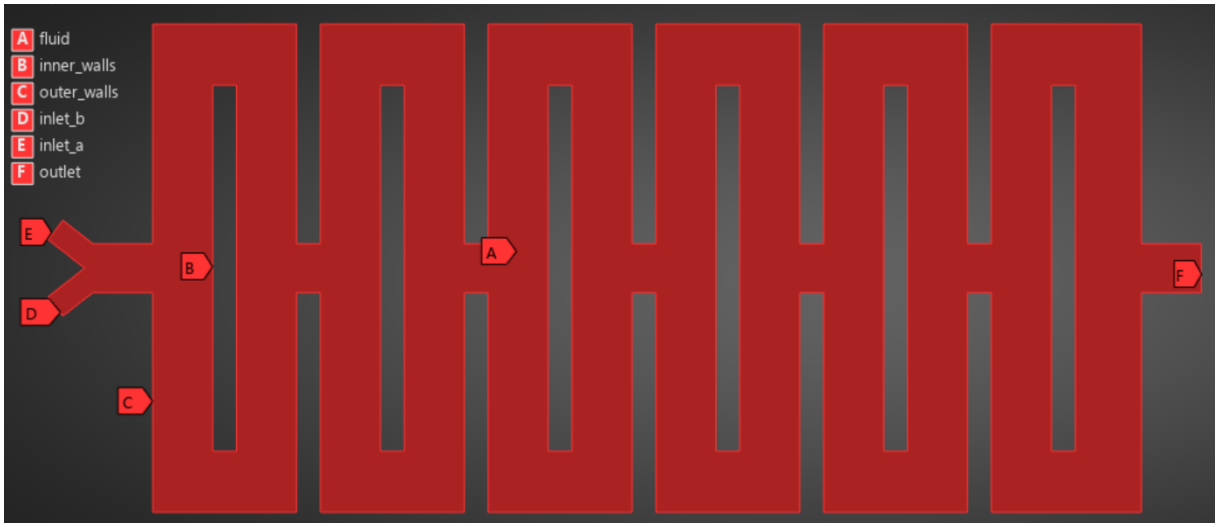

Figure 3-3: Named selections used in mesh creation.

With the initial mesh element size set and the named selections created, the first version of the mesh was ready for simulation, and the mesh independence test was carried out in Fluent®, using the settings shown in figure 3-4. At the end of this test, an adequate mesh element size was determined, and the standard version of the mesh to be used in the tracer simulations and in the parametric study was generated.

Setup	General	Type	Pressure-Based	
		Time	Steady	
	Models	Viscous	Realizable k-e, Enhanced Wall Treatment	
	Materials	Fluid	water-liquid	
	Boundary Conditions	Inlet	Velocity Magnitude / $m \cdot s^{-1}$	U_{inlet}
	Methods	Scheme	Coupled	
		Spatial Discretization	Gradient	Least Squares Cell Based
			Pressure	QUICK
			Momentum	QUICK
			Turbulent Kinetic Energy	QUICK
			Turbulent Dissipation Rate	QUICK
		Pseudo Time Method	Global Time Step	
Solution	Monitors	Residuals	continuity	10^{-5}
			x-velocity	10^{-5}
			y-velocity	10^{-5}
			k	10^{-5}
			epsilon	10^{-5}
	Initialization	Hybrid Initialization		
	Calculation	Number of Iterations	500	

Figure 3-4: Fluent® settings used for the mesh independence tests.

3.2. Tracer simulations

Tracer experiments are an important tool in reactor engineering which quantify the hydrodynamic features of a reactor. By injecting a tracer species and measuring its concentration at the reactor outlet over time, the residence time distribution (RTD) can be determined. The RTD characterizes how long fluid elements spend inside the reactor and reflects deviations from ideal flow behaviour, such as mixing inefficiencies, preferential flow paths, or stagnant regions [11].

This distribution can be used to develop simplified reactor models, using ideal plug-flow or perfectly mixed reactor approximations. From the RTD, the mean residence time, $\overline{t_r}$, can be calculated, which is the average time a fluid element spends inside the reactor.

Comparison of $\overline{t_r}$ to reactor space-time, τ, calculated using reactor volume, V, and inlet flow rate, Q, as defined in the following equation:

$$\tau = \frac{V}{Q} \tag{3-1}$$

alongside RTD curve analysis allows identification and quantification of reactor features. Specifically, $\overline{t_r} > \tau$ can indicate preferential paths, while $\overline{t_r} < \tau$ and the presence of long tails in the RTD curve can indicate stagnant zones [12].

By using CFD, tracer experiments can be replicated numerically to predict RTD curves, which can then be validated using physical tracer experiments in a 3D printed reactor, for instance [13].

These simulations were carried out, replicating tracer experiments with a step input and the numerical data was used to obtain the predicted RTD curve.

Since these experiments imply variations with time, the simulations should be performed in a transient state, and appropriate settings are required. Tracer simulations with a step perturbation were conducted at the initial planned velocities used in the parametric study for a total duration of 5τ, using the settings shown in figure 3-5, noting that the tracer species, A, has the same physical properties of liquid water.

Setup	General	Type	Pressure-Based		
		Time	Transient		
	Models	Energy	On		
		Viscous	Laminar		
		Species Model	Species Transport		
	Materials	Mixture-Template	Species	water-liquid	
				a	
			Density / $kg \cdot m^{-3}$	volume-weighted-mixing-law	
			Cp / $J \cdot kg^{-1} \cdot K^{-1}$	mixing-law	
			Thermal Conductivity / $W \cdot m^{-1}K^{-1}$	mass-weighted-mixing-law	
			Viscosity / $kg \cdot m^{-1}s^{-1}$	mass-weighted-mixing-law	
			Mass Diffusivity / m^2s^{-1}	10^{-9}	
	Boundary Conditions	Inlet	Velocity Magnitude / $m \cdot s^{-1}$	U_{inlet}	
			Temperature / K	300	
			Mass Fraction	water-liquid	0
				a	1
Solution	Methods	Scheme	Coupled		
		Spatial Discretization	Gradient	Least Squares Cell Based	
			Pressure	QUICK	
			Momentum	QUICK	
			Turbulent Kinetic Energy	QUICK	
			Turbulent Dissipation Rate	QUICK	
			a	QUICK	
			Energy	QUICK	
		Transient Formulation	Second Order Implicit		
	Monitors	Residuals	continuity	10^{-5}	
			x-velocity	10^{-5}	
			y-velocity	10^{-5}	
			energy	10^{-6}	
			k	10^{-5}	
			epsilon	10^{-5}	
			a	10^{-5}	
	Initialization	Steady state simulations in the fluid domain			
	Calculation	Type	Adaptive		
		Courant	1		
		Total Time	5τ		
		Max Iterations/Time Step	50		

Figure 3-5: Fluent® settings used for the tracer experiments.

One of the most critical settings for accurate transient simulations is the time step, i.e., the advancement in time between each calculated state. A step that is too large leads to severe inaccuracies on the simulation results, and one too small creates increased computational cost unnecessarily.

To tackle this, the dimensionless Courant Number, Co, is used, representing the ratio of the time step size to the characteristic time taken for fluid to flow through a given control volume [8]. It is calculated using Eq. 3-2:

$$Co = \frac{U\Delta t}{\Delta h} \tag{3-2}$$

where U is a characteristic flow velocity, Δt is the time step and Δh is the mesh element size. When $Co \leqslant 1$, a fluid element moves through, at most, one mesh element per time step. This contributes to the stability of the simulation and the reliability of the results [8]. For this work, a value of $Co = 1$ was chosen and used to continuously update the time step value during the simulations (using the variable time step option).

With all parameters prepared for the transient simulation, a steady state simulation is used as a starting point for the transient simulation, introducing only water into the reactor.. This initial simulation establishes a steady flow field that allows an inlet step perturbation without affecting reactor hydrodynamics. After completion, the obtained steady state flow field is kept and the inlet is changed to introduce only the tracer species, changing the inlet mass fraction of A to 1.

At this point, the transient simulation is started. At each time step, and based on the numerical "raw data", the average outlet concentration of tracer is calculated and recorded in a file, alongside the corresponding time step. Additionally, for one tracer experiment, frames of the tracer mass fraction field at 0.01 second intervals were continuously collected and used to create an animation to visualise the temporal progression of the tracer in the system.

Based on the results obtained for the temporal evolution of the average outlet tracer concentration, the Danckwerts *F(t)* and *E(t)* (i.e. RTD) curves can be easily built and used to calculate $\overline{t_r}$ (through Eqs. 3-3, 3-4, 3-5).

$$F(t) = \frac{C_s(t)}{C_{inlet}} \tag{3-3}$$

$$E(t) = \frac{dF(t)}{dt} \tag{3-4}$$

$$\overline{t_r} = \int_0^\infty t \cdot E(t) \tag{3-5}$$

C_{inlet} and C_s are the reactor inlet concentration and outlet concentration, respectively. Since the tracer species has the same properties of water (specifically for this calculation, density and molar mass), the ratio between inlet and outlet concentration is equal to the ratio of inlet and outlet tracer mass fraction. As such, *F(t)* is instead calculated by substituting tracer concentrations with the corresponding molar fractions.

3.3. Parametric study

To simplify the parametric study, Workbench was used to automate the set of steady state simulations to perform by defining input and output parameters in Fluent®. These parameters are accessed in the parameter set Workbench function, available after creation of any parameter in the Fluent® interface. The values of the input parameters can be set in a table where each row corresponds to a design point, i.e., to different cases, as shown in figure 3-6.

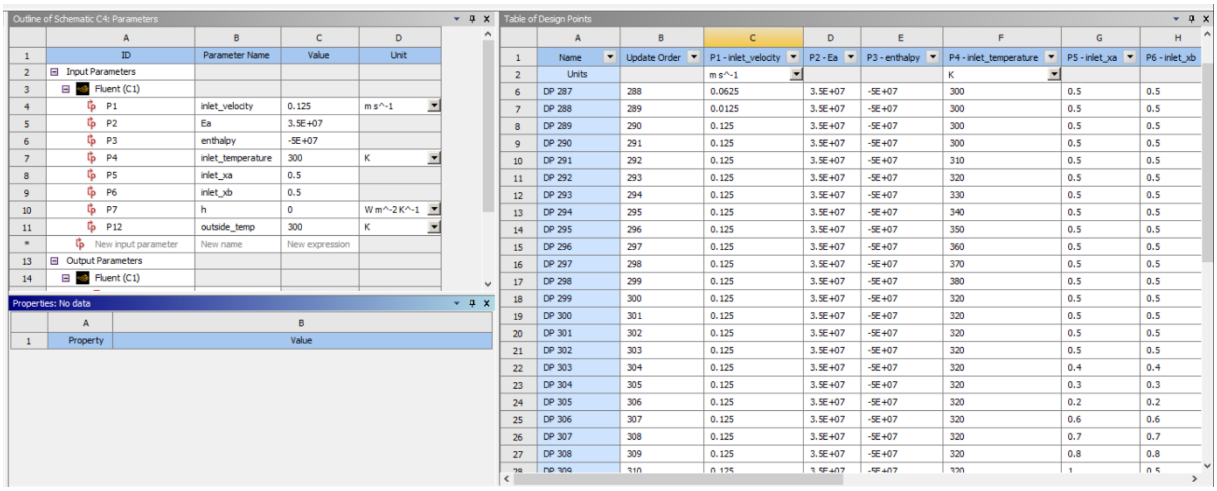

Figure 3-6: Workbench parameter set table.

The design points can be updated individually or simultaneously, associating the produced Fluent® case and data files to each specific design point. This means that although only certain variables may be assigned as output parameters, if other variables become relevant after simulation, these can still be accessed. By setting a design point as "current" in the parameter set interface, solution data can be opened in Workbench, which then opens the relevant case and data files in Fluent®.

The base settings for the steady state simulations in the parametric study were the same as the ones used in the mesh independence test, with the addition of a homogeneous exothermic reaction, $A + B \rightarrow 2C$, as well as heat transfer through the outer walls of the reactor. Settings are shown in figure 3-7.

Setup	General	Type	Pressure-Based		
		Time	Steady		
	Models	Energy	On		
		Viscous	Realizable k-e, Enhanced Wall Treatment		
		Species Model	Species Transport		
			Volumetric		
			Diffusion Energy Source		
			Finite-Rate/No TCI		
	Materials	Mixture-Template	Species	a	
				b	
				c	
				water-liquid	
			Reactions	Type	Volumetric
				Nº Reactants	2
				Stoich. Coefficient a	1
				Rate Exponent a	1
				Stoich. Coefficient b	1
				Rate Exponent b	1
				Nº Products	1
				Stoich. Coefficient c	2
				Rate Exponent c	0
				Pre-exponencial factor	k_0
				Activation Energy	E_a
			Density / $kg \cdot m^{-3}$	volume-weighted-mixing-law	
			Cp / $J \cdot kg^{-1} \cdot K^{-1}$	mixing-law	
			Thermal Conductivity / $W \cdot m^{-1}K^{-1}$	mass-weighted-mixing-law	
			Viscosity / $kg \cdot m^{-1}s^{-1}$	mass-weighted-mixing-law	
			Mass Diffusivity / m^2s^{-1}	10^{-9}	
	Boundary Conditions	Inlet	Velocity Magnitude / $m \cdot s^{-1}$	U_{inlet}	
			Temperature / K	T_{inlet}	
			Mass Fraction	a	x_a
				b	x_b
		outer_walls	Thermal Conditions	Convection	
			Heat Transfer Coefficient	h	
			Free Stream Temperature	$T_{outside}$	
Solution	Methods	Scheme	Coupled		
		Spatial Discretization	Gradient	Least Squares Cell Based	
			Pressure	QUICK	
			Momentum	QUICK	
			Turbulent Kinetic Energy	QUICK	
			Turbulent Dissipation Rate	QUICK	
			a	QUICK	
			b	QUICK	
			c	QUICK	
			Energy	QUICK	
		Pseudo Time Method	Global Time Step		
	Monitors	Residuals	continuity	10^{-5}	
			x-velocity	10^{-5}	
			y-velocity	10^{-5}	
			energy	10^{-6}	
			k	10^{-5}	
			epsilon	10^{-5}	
			a	10^{-5}	
			b	10^{-5}	
			c	10^{-5}	
	Initialization	Hybrid Initialization			
	Calculation	Number of Iterations	500		

Figure 3-7: Fluent® settings used for the parametric studies.

Another important setting is how the initialization (initial condition of a simulation) is made when moving to the subsequent design point. The available options are using the results of the previous calculated point or the results of the one set as current in the parameter set. Generally, both work correctly; however, there are cases where design points initialise from previous non-converging points that can lead to incorrect simulations. Fluent® settings used for the parametric studies.

To fix this, design point initialisation should be set to use the current design point, and a known convergent point should be set as current in the parameter set.

Furthermore, non-converging design points are not highlighted in the parameter set, showing only the defined output parameters, which at first glance may appear normal.

To confirm, the residuals plot can be checked in Fluent®, but this requires loading case and data files point by point, which is slow. Instead, the residuals plot can be viewed directly in Workbench without needing to load Fluent® files. Unfortunately, this only works for a single design point at a time, remaining quite slow.

A faster way of checking is by defining the molar fraction of all species involved in the chemical reaction as output parameters. For example, in a non-converging case where the same molar fraction of A and B is fed to the reactor at the same flow rate, outlet molar fractions of the reagents should be equal due to reaction stoichiometry. However, in non-converging cases, these fractions are dramatically different, which provides a simple way of identifying failed simulations.

The laminar model was used when possible, and in cases where unsteady turbulence exists, the Realizable k-ε was used instead. Decreasing mesh element size and mesh inflation in near wall regions was tested to attempt to obtain convergence with the laminar models but was unsuccessful. For a case where the laminar model did not converge, a comparison of the obtained velocity vectors between the laminar model and the turbulent model are shown in figure 3-8.

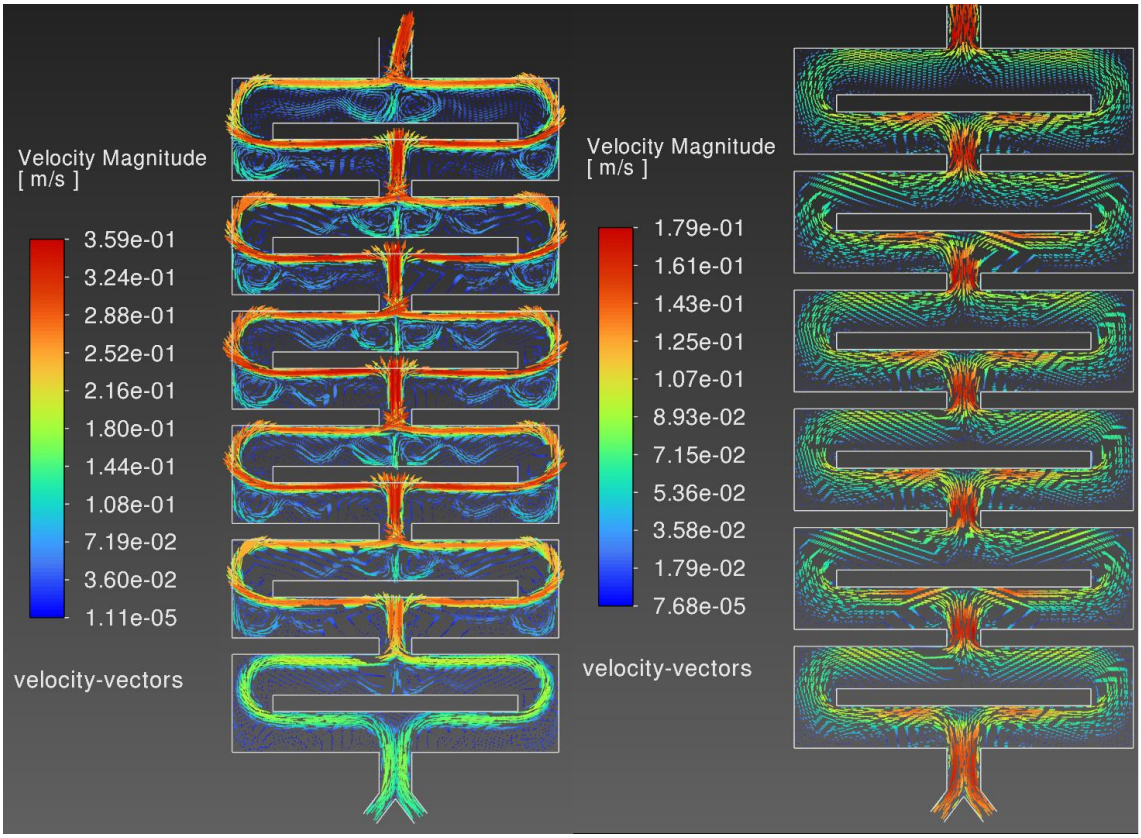

Figure 3-8: Comparison between velocity vectors while using the laminar and turbulent model, left and right, respectively.

It is important to note that the Realizable k-ε model requires suitable near wall treatment [8]. As such, the Enhanced Wall Treatment option was used in the model settings.

As with the tracer simulation, the reaction species A, B and C all have the same physical properties of liquid water, except for heat of formation.

The parameters studied were:

- Inlet Reynolds number, Re, and consequently, inlet velocity, U_{inlet}
- Inlet fluid temperature, T_{inlet}
- Inlet molar fractions of reactants A and B, $x_{a,inlet}$, $x_{b,inlet}$
- External convective heat transfer coefficient, *h*
- Temperature of the medium outside the reactor, $T_{outside}$
- Reaction enthalpy, *ΔH*
- Reaction activation energy, E_a
- Pre-exponential factor, k_0

By setting these as input parameters in Fluent® and using Workbench's parameter set functionality, almost all of these parameters can be given values in a table, and all required simulations can be executed, mostly, without further user input. The outlet concentration of each species as well as the outlet temperature are then exported directly to this table as output parameters and the data files with the complete numerical results remain accessible for detailed analysis of each case.

However, not all variables are directly assigned in Fluent® as Workbench output parameters. Specifically, the reaction parameters, k_0, E_a and *ΔH* cannot be directly added to the parameter table. To circumvent this, scheme procedures were used to run Fluent® Text User Interface (TUI) commands that accept generalized inputs set as input parameters, which can then change the desired variables. This can be done from the Fluent® parameter user interface, which is shown in figure 3-9.

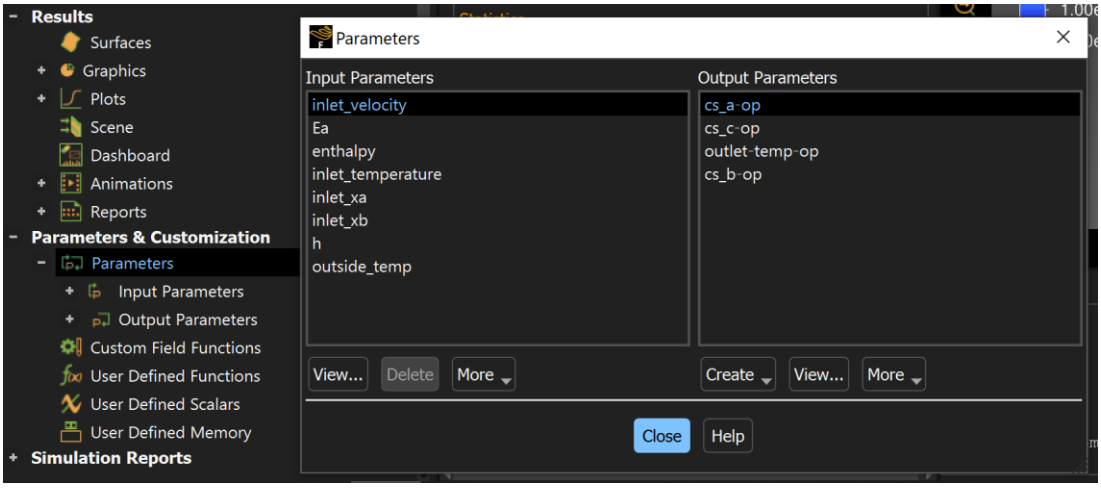

Figure 3-9: Fluent® parameters user interface.

From here, using the “More” dropdown on the left side, a scheme procedure can be created for an input parameter in the user interface shown on figure 3-10.

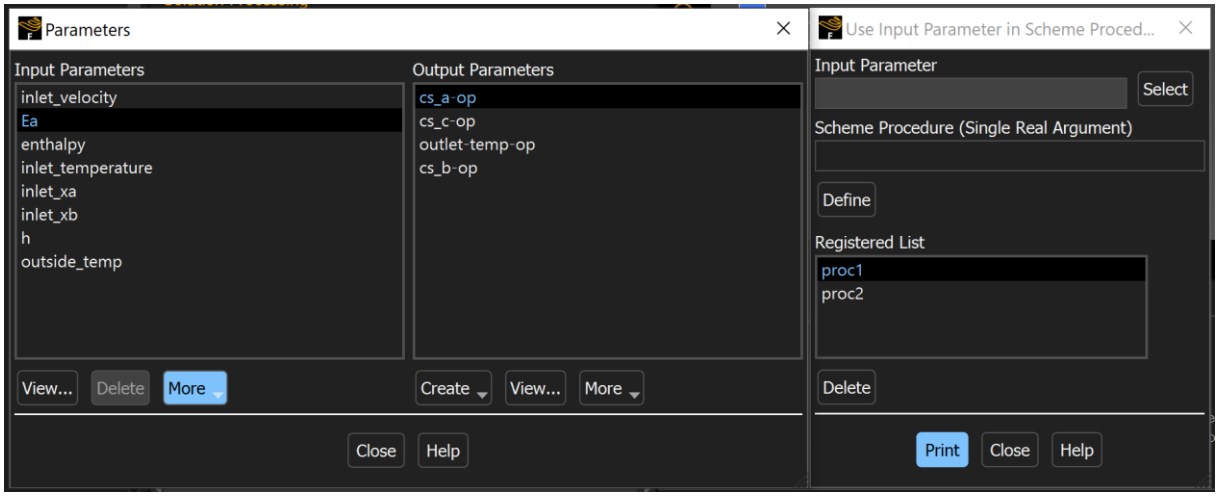

Figure 3-10: Scheme procedure user interface.

After selecting the desired input parameter to use in the procedure, a lambda function must be placed in the Scheme Procedure, which will then run the TUI command. In the case of the procedure that changes E_a values, the following lambda function is used:

```
(lambda (value) (ti-menu-load-string (args->string
   '/define/materials/change-create/mixture-template
    'mixture-template _ 'yes '1 'reaction-1 _ _ _ _ '2 'a '1 '1 'b '1 '1 '1 'c '2 '0 '1 value '0 _ _ _ _ _ _ _ _ _ _
)))
```

In Fluent®, the lambda function should be a single line, but for ease of explanation it is separated into several lines.

The first line of the command, where the lambda function is defined and the “ti-menu-load-string” command is called, is responsible for changing Fluent® settings from a given text string, where “value” will be replaced by the input parameter used in the procedure.

The next line, beginning in “/define”, navigates the TUI menu structure to reach the mixture-template settings and at this point Fluent® requests values to create or modify the mixture-template.

This is done with the final line of the function, using numbers, strings, and a series of underscores, which represent default values. Following the command, a “reaction-1” is created with 4 default values (‘reaction-1 _ _ _ _). After this, the number of reagents is set, 2 for species A and B, followed by their name, stoichiometric coefficient and reaction order, repeating for each reagent ('2 'a '1 '1 'b '1 '1 '1) and then the product ('c '2 '0 '1).

E_a is set by the "value" string, which is the value provided to the lambda function in the first line, the input parameter. The next settings are set to their defaults, and the scheme procedure finishes.

Unfortunately, and as can be seen in parenthesis in the scheme procedure user interface, Fluent® scheme procedures can only have a single real argument per scheme, and since k_0 and E_a are both set with the same command, one of these needs to be set manually.

As k_0 is planned to change less frequently than E_a, the pre-exponential factor is set manually.

Reaction enthalpy is not directly defined, as it is calculated from the formation enthalpy and stoichiometry of each material in each reaction. Due to the single argument restriction, the formation enthalpy of species A and B is set to zero, and the scheme procedure changes only the enthalpy of species C.

4. Results and Discussion

The main purpose of this work was to perform an extensive parametric study in an illustrative non-isothermal reactor using the numerical workflow outlined previously. This study addressed a hypothetical exothermic reaction and analysed the effect of different parameters on conversion and temperature throughout the reactor and at the outlet.

4.1. Mesh Independence Test

As mentioned in the methodology, the mesh independence test is crucial to determine an acceptable mesh element size to be used in the following simulations. The present work involved a range of the inlet Reynolds number from 100 to 2000, and the corresponding velocities at the inlet boundaries were calculated using the viscosity and density of the fluid, μ and ρ, and the combined length of the inlets, D. All values are shown in table 4-1 and will be used over the course of the work.

Table 4-1: Velocities obtained from the inlet Reynolds number, fluid properties and combined inlet length.

Re_{inlet}	ρ / kg·m^{-3}	D / cm	μ / $Pa \cdot s$	U_{inlet} / m·s^{-1}
2000	$1 \cdot 10^3$	0.8	$1 \cdot 10^{-3}$	$2.5 \cdot 10^{-1}$
1500				$1.875 \cdot 10^{-1}$
1000				$1.25 \cdot 10^{-1}$
500				$6.25 \cdot 10^{-2}$
100				$1.25 \cdot 10^{-2}$

In accordance with the defined methodology, the system with the highest inlet velocity was used for the mesh independence test. The results obtained for the average velocity, calculated as the area-weighted average in Fluent®, the velocity profiles at the outlet boundary, and the relative error in comparison to the previous point, are shown in table 4-2 and figure 4-1, respectively.

Table 4-2: Average outlet velocities obtained from the mesh independence test.

Mesh	Δh / m	U_{outlet} / m·s^{-1}	Relative Error (%)
1	$1.25 \cdot 10^{-3}$	0.25027	
2	$6.25 \cdot 10^{-4}$	0.25021	0.0241
3	$3.125 \cdot 10^{-4}$	0.25007	0.0569
4	$1.5625 \cdot 10^{-4}$	0.25004	0.0099

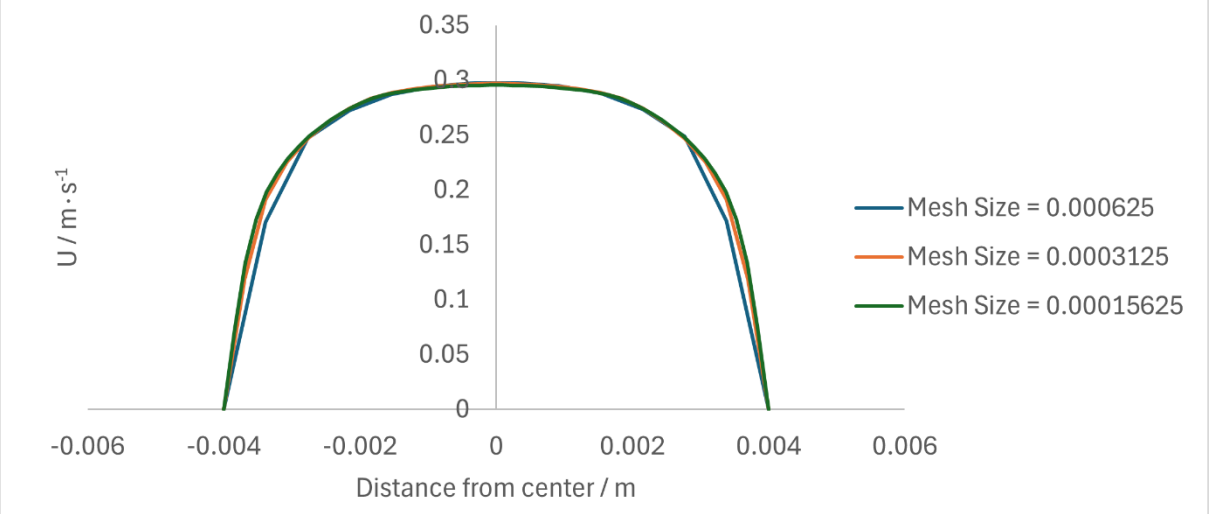

Figure 4-1: Velocity profiles at reactor outlet.

As the mesh element size decreases, U_{outlet} decreases as well, approaching the inlet value of 0.25 m·s⁻¹, which is expected as the outlet has the same length as *D*. As the obtained U_{outlet} values are quite similar for meshes 3 and 4, with a relative error below 0.01%. In addition, the velocity profiles between mesh 2 and 3 show a discrepancy in the near wall regions of the outlet, which is reduced when comparing mesh 3 and 4. Mesh 3 was chosen to be used over the course of the work as a compromise between accuracy, which remains unaffected when compared to using mesh 4, and computational cost, as the decreased mesh element size will always lead to higher simulation completion times.

4.2. Tracer simulations

Following the methodology described in section 3.2, the value of τ and 5τ were obtained from the flow rate corresponding to each inlet velocity and from the reactor volume, both of which are obtained directly in Fluent®, using the Fluxes and Volume Integral functionality (Fluent® assumes a default reactor depth of 1 m), respectively. The obtained and calculated values are shown in table 4-3.

Table 4-3: Tracer simulation parameters.

U_{inlet} (m/s)	Q / m³·s⁻¹	V / m³	τ / s	5τ / s
$2.5 \cdot 10^{-1}$	$2 \cdot 10^{-3}$	$1.048 \cdot 10^{-2}$	5.271	26.35
$1.875 \cdot 10^{-1}$	$1.5 \cdot 10^{-3}$		7.028	35.14
$1.25 \cdot 10^{-1}$	$1 \cdot 10^{-3}$		10.54	52.71
$6.25 \cdot 10^{-2}$	$5 \cdot 10^{-4}$		21.08	105.4
$1.25 \cdot 10^{-2}$	$1 \cdot 10^{-4}$		105.4	527.1

Using these values, the tracer simulations were executed, and the following *F(t)* and *E(t)* curves were built using Eqs. 3-3, 3-4 and are shown in figures 4-2 to 4-6.

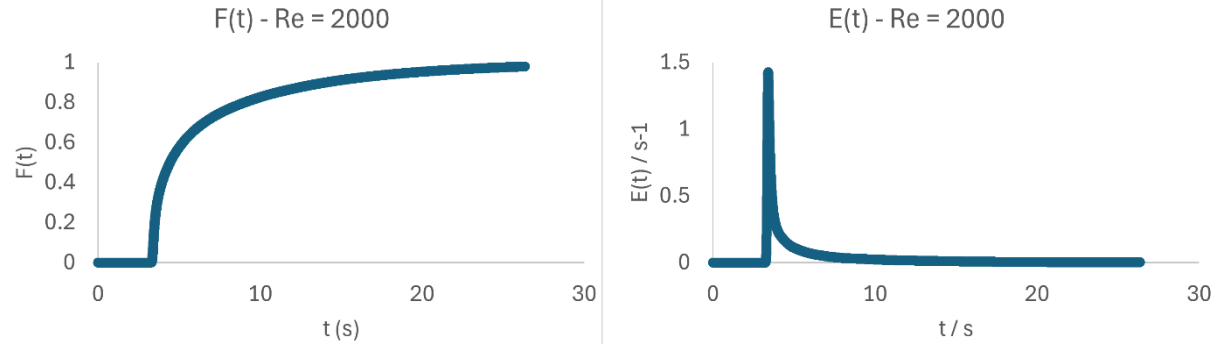

Figure 4-2: F(t) and E(t) curves for Re = 2000.

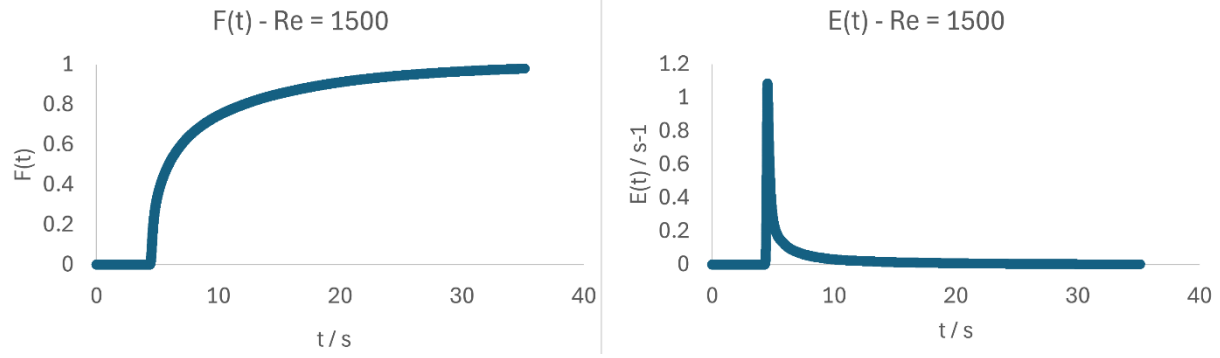

Figure 4-3: F(t) and E(t) curves for Re = 1500.

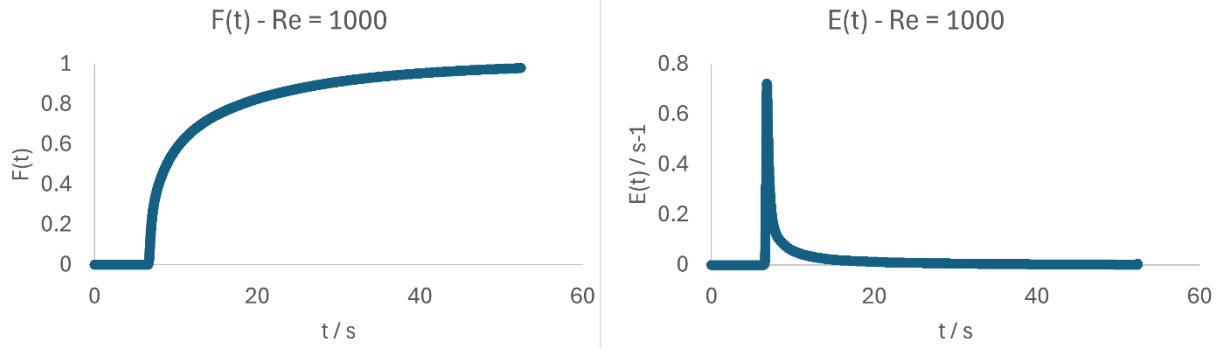

Figure 4-4: F(t) and E(t) curves for Re = 1000.

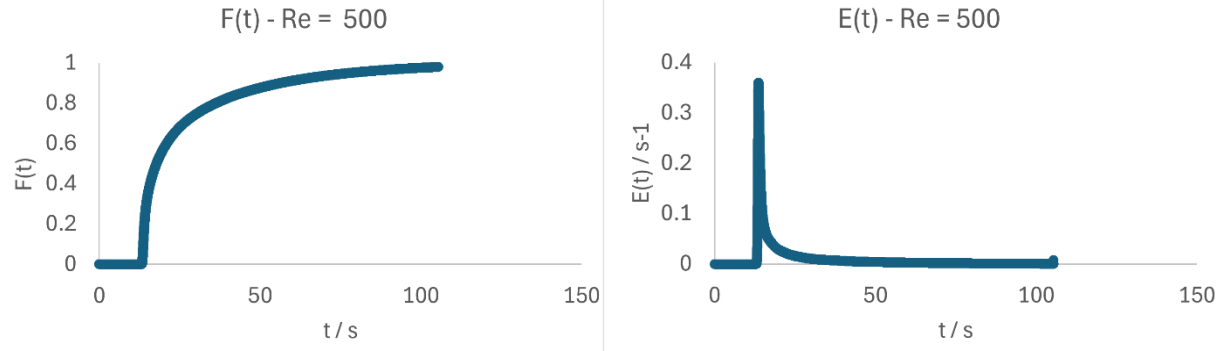

Figure 4-5: F(t) and E(t) curves for Re = 500.

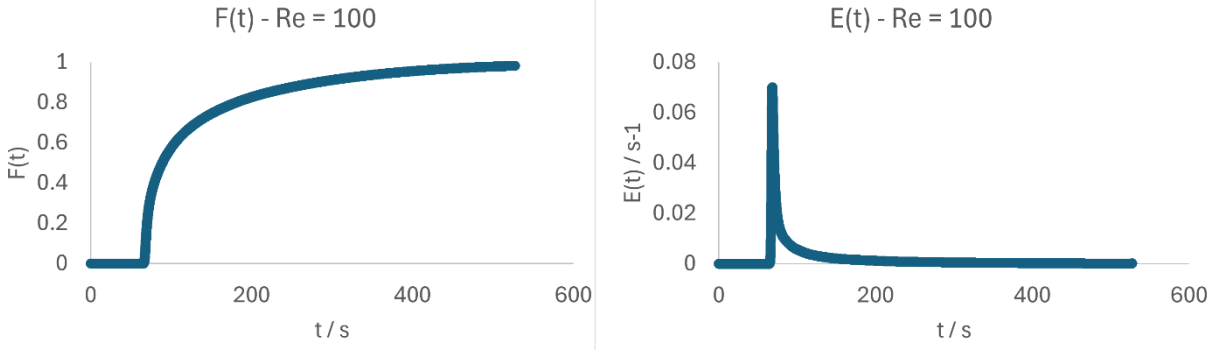

Figure 4-6: F(t) and E(t) curves for Re = 100.

With the *E(t)* curves, the mean residence time can be calculated through Eq. 3-5. The corresponding results for each inlet velocity and Reynolds value are shown in table 4-4.

Table 4-4: Space-time and mean residence time for each Reynolds value

Re_{inlet}	U_{inlet} / m·s^{-1}	τ / s	$\overline{t_r}$ / s
2000	$2.5 \cdot 10^{-1}$	5.270	6.282
1500	$1.875 \cdot 10^{-1}$	7.028	8.379
1000	$1.25 \cdot 10^{-1}$	10.54	12.55
500	$6.25 \cdot 10^{-2}$	21.08	25.18
100	$1.25 \cdot 10^{-2}$	105.4	126.7

In all cases, $\overline{t_r}$ values are greater than τ, an indication of the presence of preferential paths in the reactor geometry.

4.3. Parametric study

As elaborated in the methodology, the parametric study uses a theoretical homogeneous liquid phase reaction, $A + B \rightarrow 2C$, where A, B and C are defined in accordance with the methodology outlined in section 3.3. The reaction kinetics is of first order for each reagent, and the kinetic constant follows the Fluent® finite-rate kinetic model, the modified Arrhenius law [6], shown in Eq. 4-1:

$$k = k_0 \cdot T^{\beta} \cdot exp\left(\frac{-E_a}{R_g \cdot T}\right) \quad (4\text{-}1)$$

where *k* is the rate constant for the reaction, k_0 is the pre-exponential factor, β is the temperature exponent, set to zero in all studies, E_a is the activation energy, R_g is the ideal gas constant and *T* the absolute temperature.

The reactants enter through the reactor inlets, one for each reactant. In cases where reactor inlets are not pure (i.e, A and B molar fractions lower than 1), the remainder of the feed is inert liquid water.

A large set of simulations were carried out to address the influence of several parameters - relating to inlet conditions, kinetics and heat transfer - on outlet average molar fraction of the product, x_c, and outlet average temperature, T_{outlet}. In total, around 800 simulations were performed. Of these, a large portion used reaction parameters from a previous thesis, [13], and the corresponding discussion is available in Appendix B, due to unrealistic temperature values.

4.3.1. Inlet velocity

The first study revolves around the variation of U_{inlet}, and consequently of the inlet flow rate. The velocity values used were equal to those used in the tracer experiments. The remaining parameters are detailed in table 4-5, and the obtained x_c and T_{outlet} are shown in figure 4-7. It is important to note that the two reactor inlets feed species A and B, respectively, and the remaining 50% in both inlets is an inert species, liquid water.

Table 4-5: Reaction parameters and boundary conditions for the inlet velocity study.

k_0 / $m^3 \cdot kmol^{-1}s^{-1}$	E_a / kJ ·mol^{-1}	ΔH / kJ ·mol^{-1}	T_{inlet} / K	$x_{a,inlet}$	$x_{b,inlet}$
500	35	-50	300	0.5	0.5

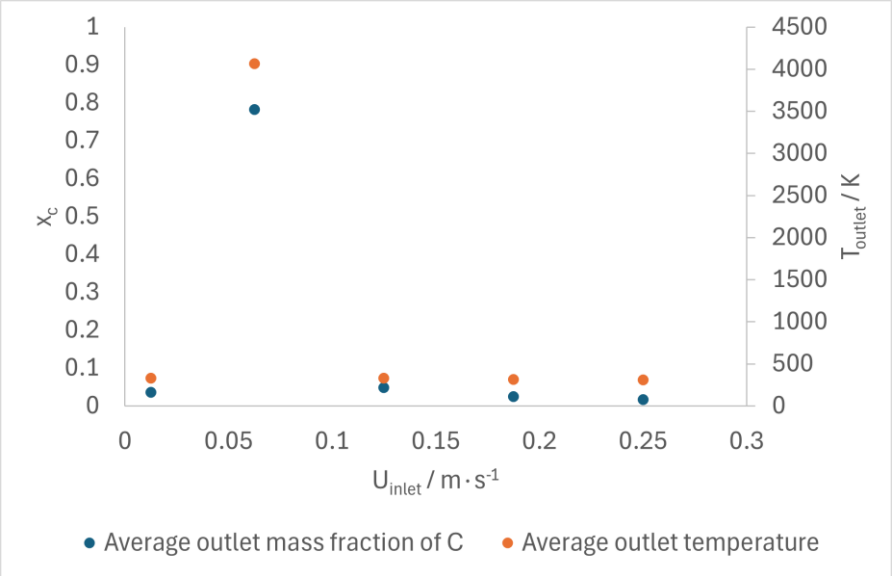

Figure 4-7: x_c and T_{outlet} for each velocity.

Generally, the results follow expectations. As inlet velocity decreases, so does the flow rate, leading to larger residence times, which should benefit conversion. This is true for the first three higher velocity points as molar fraction of C increases, although very slowly, along with the outlet temperature.

Even in adiabatic operation, the fluid is unable to heat up due to chemical reaction for these relatively small residence times, which results in the similar outlet values despite U_{inlet} variation.

For $U_{inlet} = 6.25 \cdot 10^{-2}\ m \cdot s^{-1}$, the obtained results deviate from expectations. Temperature increases excessively, reaching unrealistic temperature values. At this flow rate, enough heat is released so that reaction rates increase significantly in a small area, causing temperature values to spike in value, a phenomenon known as thermal runaway.

Estimated temperatures quickly reached the maximum defined in Fluent®, 5000 K, leading to non-converging cases due to oscillatory behaviour, as shown in figure 4-8.

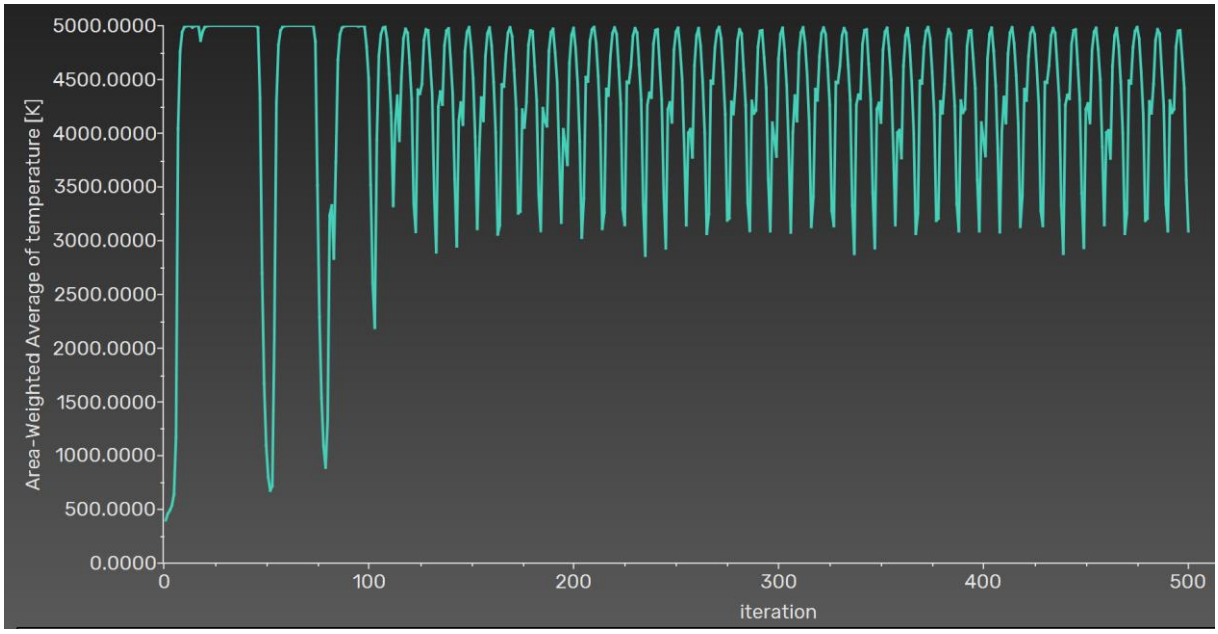

Figure 4-8: Outlet temperature plot of a non-converging case.

This temperature limit can be increased, which would allow for convergence in these cases. However, as this limit is already extremely unrealistic, increasing it would make it more so. Reaching the defined limit while performing a steady state simulation is interpreted as an indication of thermal runaway, identified in the oscillatory behaviour of temperature and residuals plots, shown in figure 4-9, as Fluent® attempts to reduce temperature values to achieve convergence.

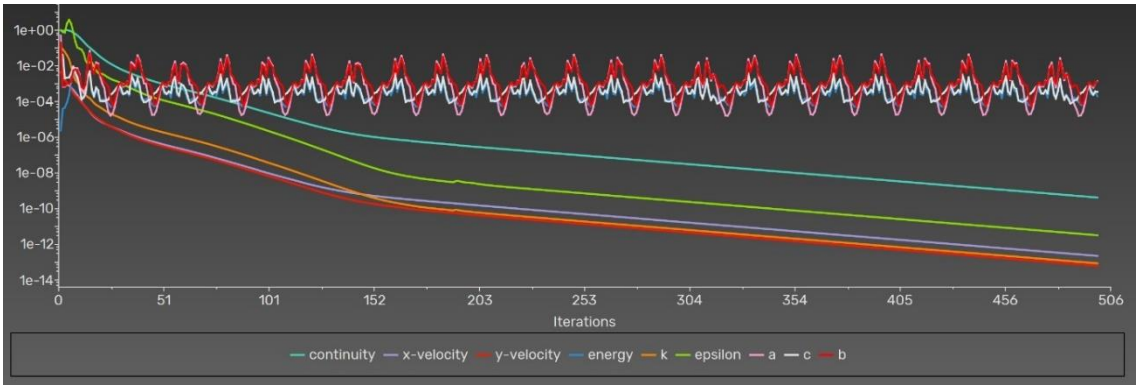

Figure 4-9: Residuals plot of a non-converging case.

Surprisingly, thermal runaway does not occur for $U_{inlet} = 1.25 \cdot 10^{-2}\ m \cdot s^{-1}$, which would be expected due to increased residence time. The obtained values are closer instead to the

higher velocity cases. Comparison between molar fraction contours of this case and others in the next section, 4.3.2, shows that the reason for this discrepancy is caused by reduced reagent mixing due to lack of turbulence, which reduces overall production and heat release.

4.3.2. Reagents mixing

Following the observations made in the previous subchapter, chemical reaction was disabled to exclusively study reagents mixing throughout the reactor, feeding pure A in one inlet and pure B in the other. The molar fraction contours of A obtained for a value of U_{inlet} from $1.875 \cdot 10^{-1}$ m·s^{-1} to $1.25 \cdot 10^{-2}$ m·s^{-1}, are shown in figure 4-10. A gradual decrease in mixing can be seen from left to right, and the biggest difference occurs from $6.25 \cdot 10^{-2}$ m·s^{-1} to $1.25 \cdot 10^{-2}$ m·s^{-1}, due to transition into laminar flow. To better visualise this transition, simulations were also performed with additional intermediate points between these two velocities, and the results of molar fraction contours of A are shown in figure 4-11.

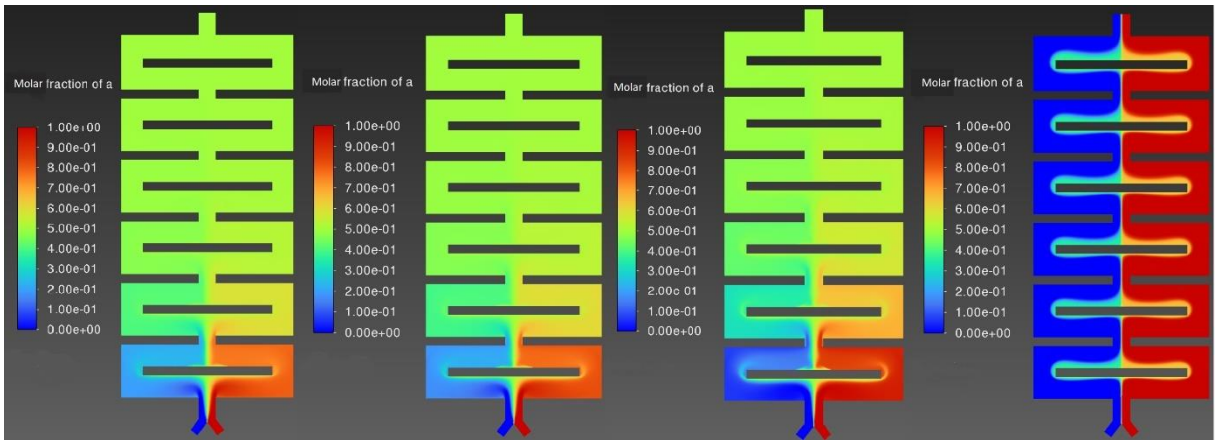

Figure 4-10: Molar fraction contours of A, U_{inlet} = $1.875 \cdot 10^{-1}$, $0.125 \cdot 10^{-1}$, $6.25 \cdot 10^{-2}$, $1.25 \cdot 10^{-2}$ m·s^{-1}, left to right, respectively.

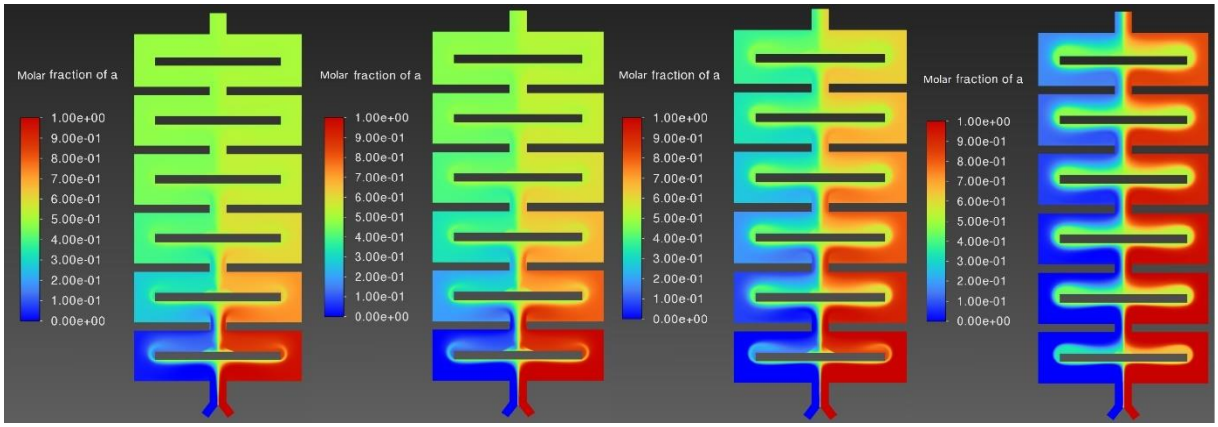

Figure 4-11: Molar fraction contours of A for intermediate U_{inlet} points, U_{inlet} = $5 \cdot 10^{-2}$, $3.75 \cdot 10^{-2}$, $2.5 \cdot 10^{-2}$, $1.875 \cdot 10^{-2}$ m·s^{-1}, left to right, respectively.

For low velocities, mass transfer occurs mainly through diffusion due to the absence of turbulence, which results in a clear separation of zones rich in species A and B. In higher velocity cases this behaviour is absent, as turbulence intensifies mass transfer, promoting mixing.

As velocity decreases, the contribution to mass transfer due to turbulence decreases as well and the obtained contours look similar to the laminar flow cases, with more pronounced separation.

These differences impact the reaction, as high mixing cases can be controlled by reaction rate, while low mixing cases are controlled by the diffusion of species from each separate zone, which explains the behaviour observed in the previous subchapter: for $U_{inlet} = 6.25 \cdot 10^{-2}\, m \cdot s^{-1}$, the residence time combined with sufficient mixing results in a case that is controlled by reaction kinetics that causes thermal runaway; meanwhile, for $U_{inlet} = 1.25 \cdot 10^{-2}\, m \cdot s^{-1}$, the lack of proper mixing controls the case, impeding runaway even though the residence time is increased.

4.3.3. Inlet temperature

Knowing that cases with sufficient mixing can be controlled by reaction kinetics, increasing inlet temperature should increase conversion by promoting the reaction. As low velocity cases are controlled by mass transfer, increasing the inlet temperature should not result in a significant increase in conversion.

Simulations were performed using the parameters in table 4-6, and the obtained outlet variables are shown in figures 4-12 and 4-13, for each velocity.

Table 4-6: Reaction parameters and boundary conditions for inlet temperature study.

U_{inlet} / m·s^{-1}	k_0 / m^3·kmol^{-1}s^{-1}	Ea / kJ ·mol^{-1}	ΔH / kJ ·mol^{-1}	$x_{a,inlet}$	$x_{b,inlet}$
$1.25 \cdot 10^{-1}$	500	35	-50	0.5	0.5
$1.25 \cdot 10^{-2}$					

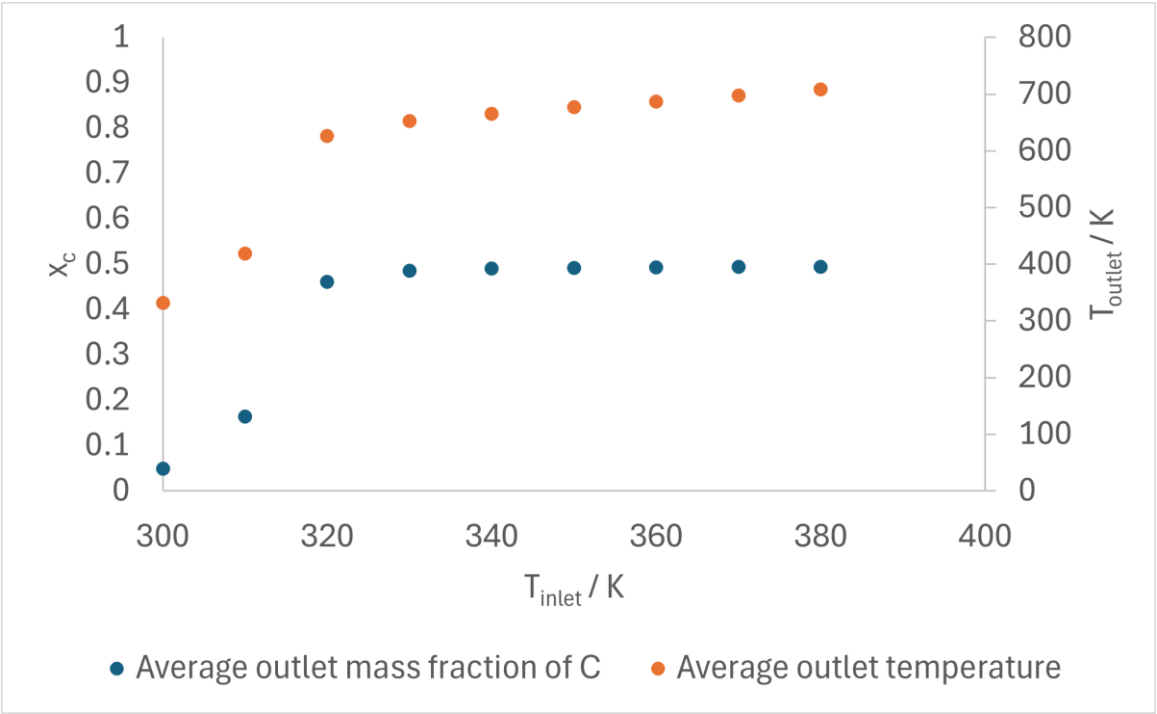

Figure 4-12: x_c and T_{outlet} for different T_{inlet} values, U_{inlet} = $1.25 \cdot 10^{-1}$ m·s^{-1}.

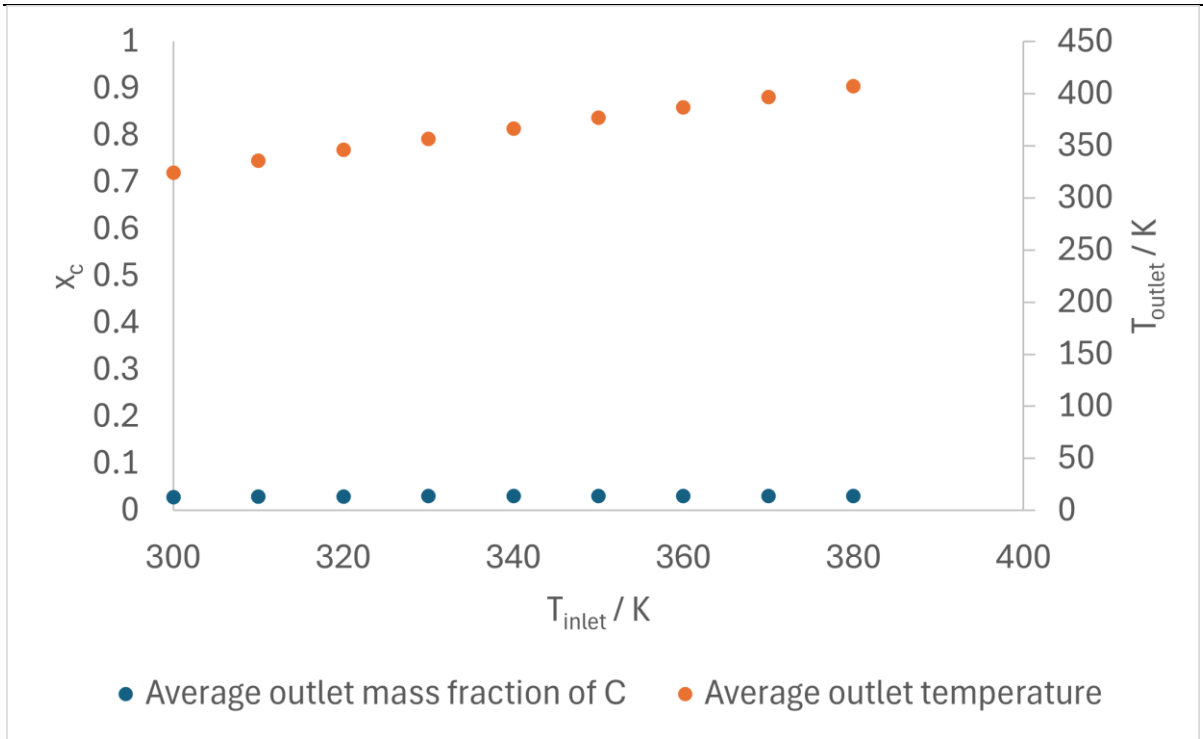

Figure 4-13: x_c and T_{outlet} for different T_{inlet} values, U_{inlet} = $1.25 \cdot 10^{-2}$ $m \cdot s^{-1}$.

As expected for the higher velocity case, increasing T_{inlet} results in improved reaction rates, resulting in higher conversion into product C and outlet temperature. Of course, values around 400 K are not realistic, as the reactants and product have similar properties to water. Still, these cases provide useful results for the parametric study, illustrating the effect of the studied variables, even if unrealistic.

From 320 K onwards x_c remains constant, representing complete reactants conversion, as x_c approaches the theoretical maximum of 0.5. As the flow from the two inlets are combined, the actual molar fraction of each reactant fed to the reactor is halved, as the 50% reactant and 50% inert feeds are combined into the single tube that feeds the main reactor zone. Following the reaction stoichiometry, in cases where $x_{a,inlet} = x_{b,inlet}$, the expected maximum value of x_c is equal to the inlet molar fractions of reactants.

Outlet temperature continues to increase in increments from 626 K to a maximum of 707 K, due to adiabatic operation and the increase in feed temperature. While no thermal runaway occurred, temperature values are still higher than ideal, especially considering the properties of the used species, equal to liquid water. Adding heat transfer to the outside of the reactor should help control reactor temperature, and inlets can be diluted further in case released heat energy remains excessive.

For the lower velocity case, although reaction rate is increased due to higher inlet temperature, no effect on conversion is observed as this case is controlled by the diffusion of reagents and not by the chemical reaction itself. As such, the obtained outlet molar fraction of the product remains very similar to the previous simulations (close to 0). As before, temperature increases incrementally due to adiabatic operation and the increase in T_{inlet}.

4.3.4. Heat transfer

Using the higher velocity case from the previous subchapter, with $T_{inlet} = 320K$, as a base, heat transfer to the outside of the reactor was added to simulations changing two variables: *h* and $T_{outside}$, the convective heat transfer coefficient of the outside medium and its' temperature, respectively.

The used parameters are available in table 4-7, while the obtained outlet variables are shown in figure 4-14.

Table 4-7: Reaction parameters and boundary conditions for the heat transfer study.

k_0 / $m^3 \cdot kmol^{-1} s^{-1}$	E_a / kJ ·mol^{-1}	ΔH / kJ ·mol^{-1}	T_{inlet} / K	$x_{a,inlet}$	$x_{b,inlet}$	$T_{outside}$ / K
500	35	-50	320	0.5	0.5	300

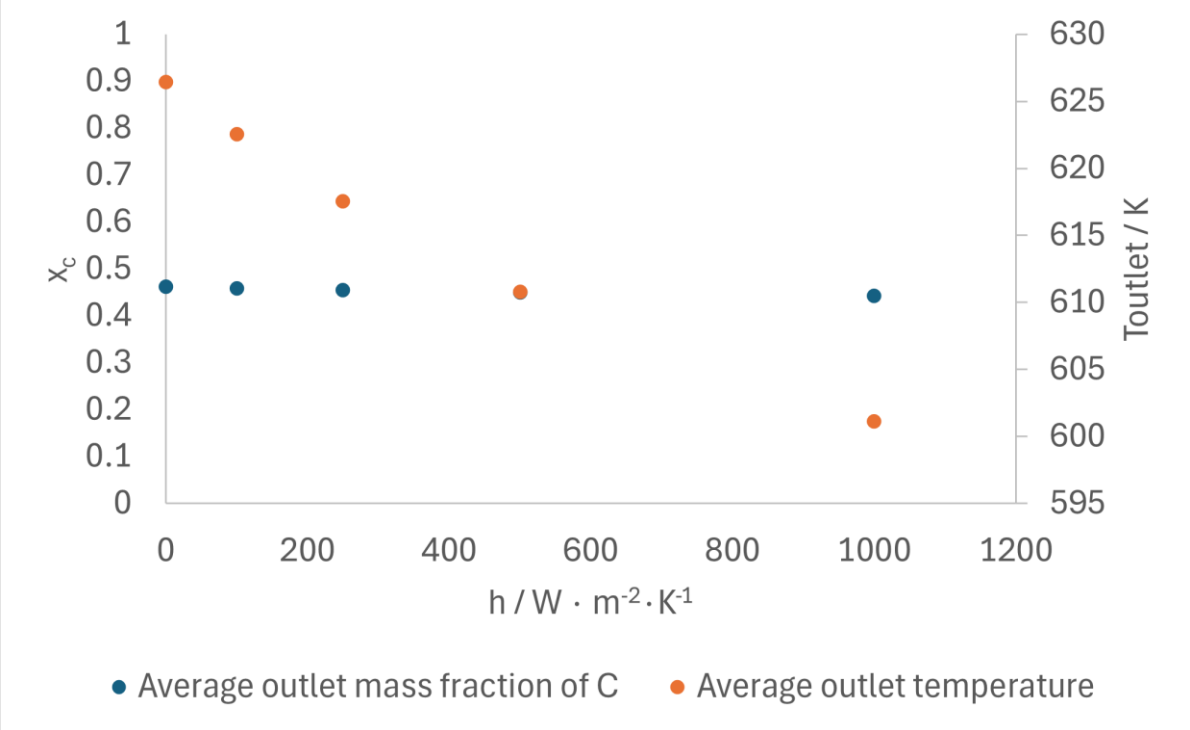

Figure 4-14: x_c and T_{outlet} for different h values, $T_{outside}$ = 300 K.

Adding heat transfer reduces outlet temperature, reducing T_{outlet} from 626 K to 601 K, while x_c maintains similar values. This is due to heat removal occuring only in near wall regions, while inner sections of the reactor maintain higher temperatures. As such, the majority of the reactor retains temperature values close to the adiabatic case, with almost no impact on conversion. Temperature contours are shown in figure 4-15, where the temperature of inner reactor sections can be observed.

Only near wall regions significantly decrease in temperature, with maximum temperature remaining high even as *h* increases.

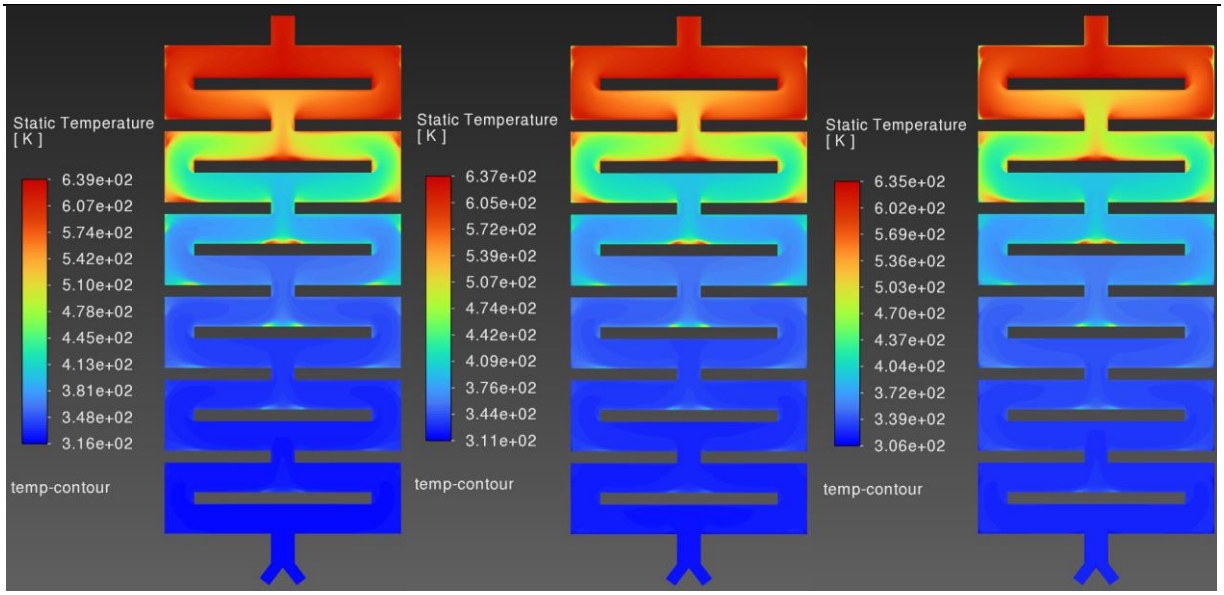

Figure 4-15: Temperature contours for different h values, 250, 500 and 1000 $W \cdot m^{-2} \cdot K^{-1}$*, respectively from left to right.*

As *h* increases, exterior heat resistance decreases as well, which improves global heat transfer. However, as mentioned, inner reactor hotspots remain at high temperature levels, with a slight decrease in maximum temperature. This highlights the need for internal cooling elements to directly cool inner zones, ideally in a counter-current arrangement to maximize heat transfer. Reactor diameter can also be reduced and length increased, leading to a higher external coolant contact area and decreased reactor-side heat transfer resistance, while maintaining reactor space-time. These changes would also be required for the study of higher reaction enthalpy values, as higher heat release would exacerbate the already problematic temperature values which would create more non-converging cases.

As an alternative to geometric changes, reactor inlets can be diluted to reduce overall reaction rate and to limit heat energy released over the course of the reactor, but this of course detrimentally affects overall production.

4.3.5. Inlet molar fractions

Based on the previous lowest T_{outlet} case, corresponding to $h = 1000\, W \cdot m^{-2} \cdot K^{-1}$, inlet molar fractions were varied in two ways: stoichiometrically, with equal fractions of A and B fed to the reactor through their respective inlets; and with one reagent in excess, to maintain reaction rate while limiting overall heat production.

Starting with the stoichiometric inlets, the obtained outlet variables are shown in figure 4-16.

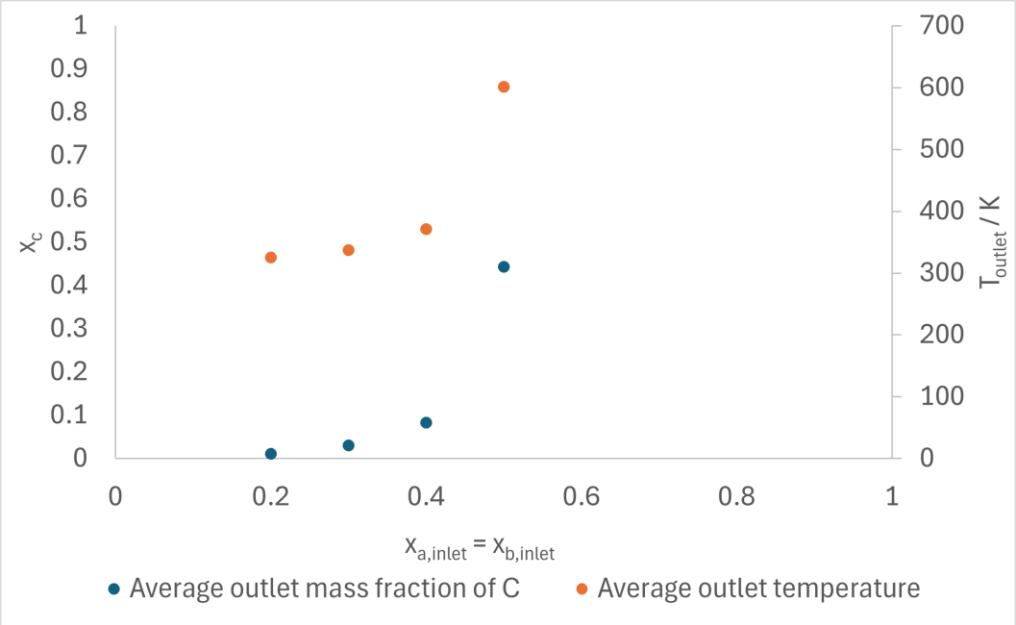

Figure 4-16: x_c and T_{outlet} for different stoichiometric inlet molar fractions

Besides the inlet molar fraction values addressed in figure 4-15, increments of 0.1 from 0.5 to 0.8 were also tested. These corresponding results are not represented in this plot because of non-convergence due to excessive temperature values.

Reducing $x_{a,inlet}$ and $x_{b,inlet}$ equally resulted in lower reaction rates, which consequently leads to lower temperature levels (and product content in the outlet stream). As such, to maintain higher reaction rates while trying to reduce overall reactor temperature, configurations with one reagent in excess, species A, fed through one of the inlets, were tested. To quantify this increase, reaction rate contours were created for two cases: $x_{a,inlet} = x_{b,inlet} = 0.3$; and $x_{a,inlet} = 1$, $x_{b,inlet} = 0.3$. These contours are shown in figure 4-17, with a higher maximum reaction rate in the reagent in excess system.

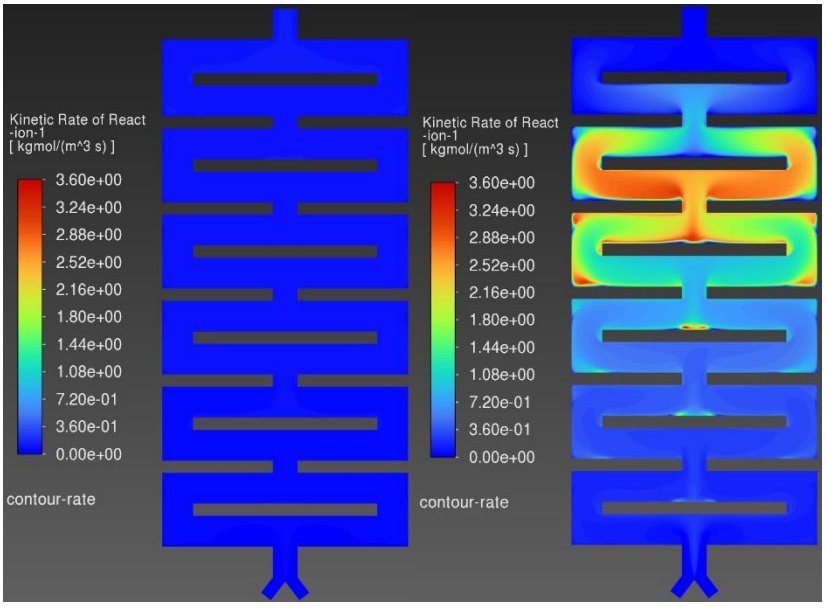

Figure 4-17: Contours of reaction rate with $x_{b,inlet} = 0.3$, for different values of $x_{a,\,inlet}$: 0.3 and 1, respectively.

Using an equal scale, the rates obtained in the first case are completely overshadowed by the second, reagent in excess case. Indeed, the volume-weighted average reaction rate increased by a factor of 10, rising from $7.89 \cdot 10^{-2}$ to $7.88 \cdot 10^{-1}$ kmol·m^{-3}·s^{-1}. Of course, this increase does lead to higher temperature values in the second case, due to higher reactant conversion, as seen in the comparison between cases shown in figure 4-18.

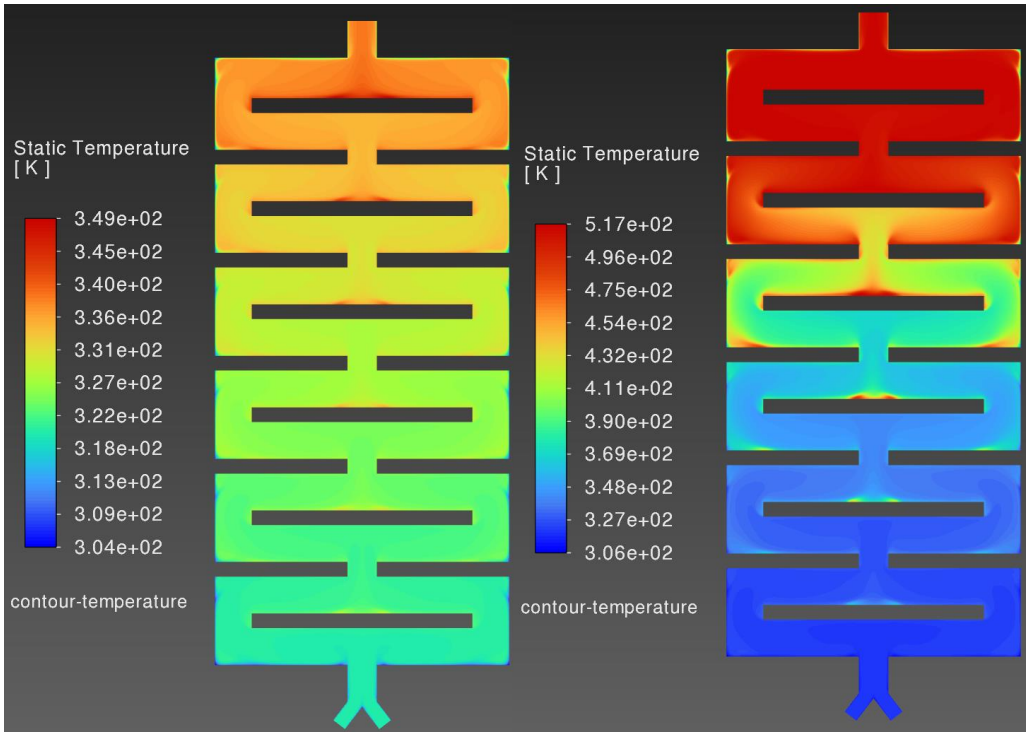

Figure 4-18: Temperature contours with $x_{b,inlet} = 0.3$, for different values of $x_{a,\ inlet}$: 0.3 and 1, respectively.

The obtained plots for variations in inlet molar fraction values of A and B are shown in figures 4-19 to 4-22. Values of $x_{b,inlet}$ from 0.5 to 0.2 were tested, and non-converging systems are excluded from the plots.

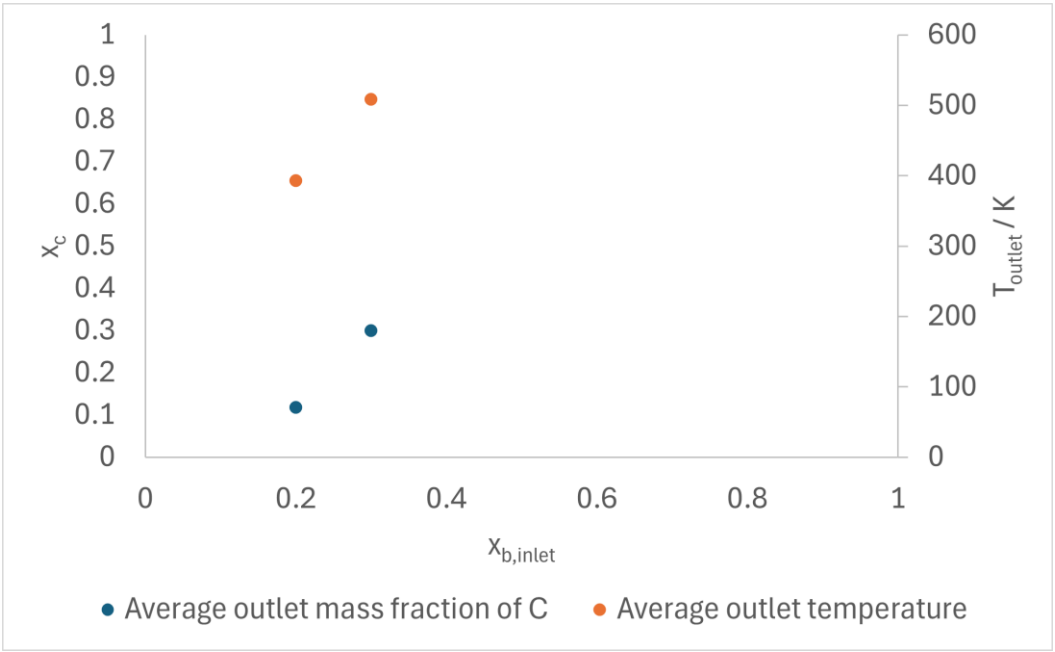

Figure 4-19: x_c and T_{outlet} for different $x_{b,inlet}$ values, $x_{a,inlet}$ = 1.

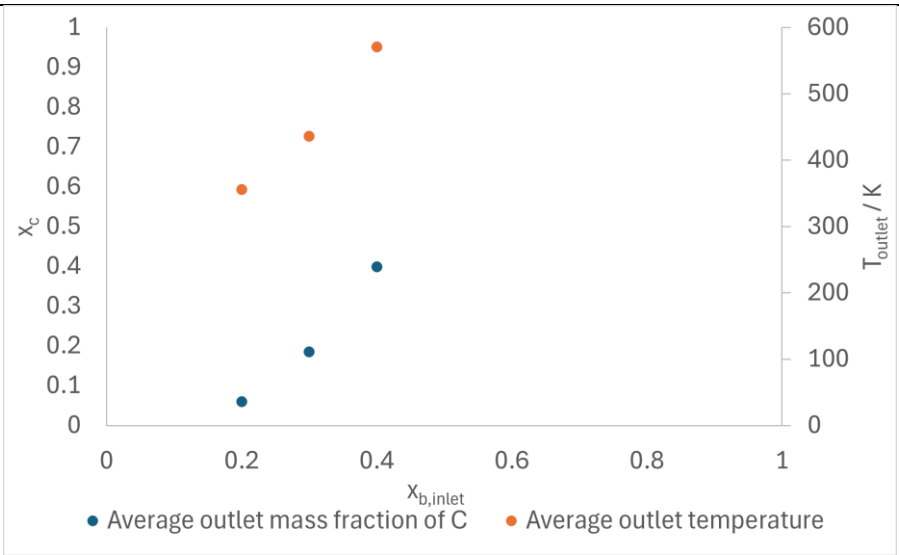

Figure 4-20: x_c and T_{outlet} for different $x_{b,inlet}$ values, $x_{a,inlet}$ = 0.7

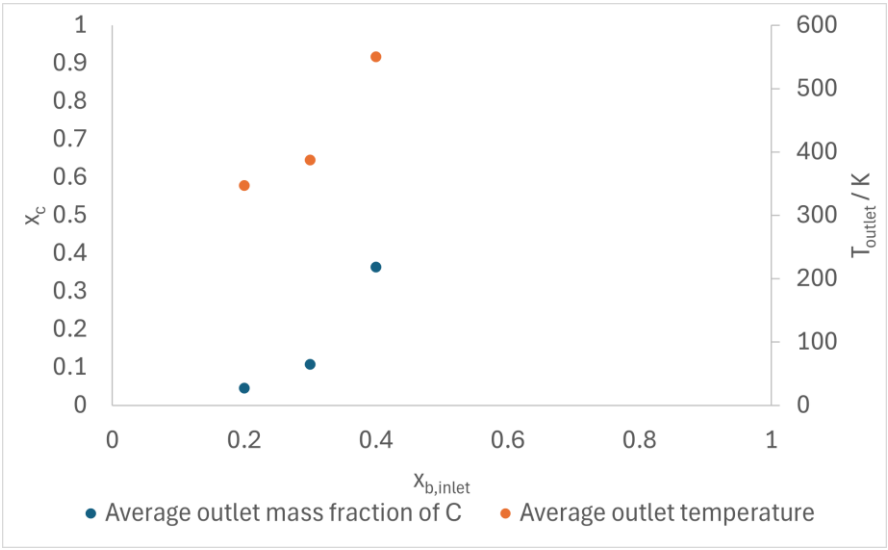

Figure 4-21: x_c and T_{outlet} for different $x_{b,inlet}$ values, $x_{a,inlet}$ = 0.6

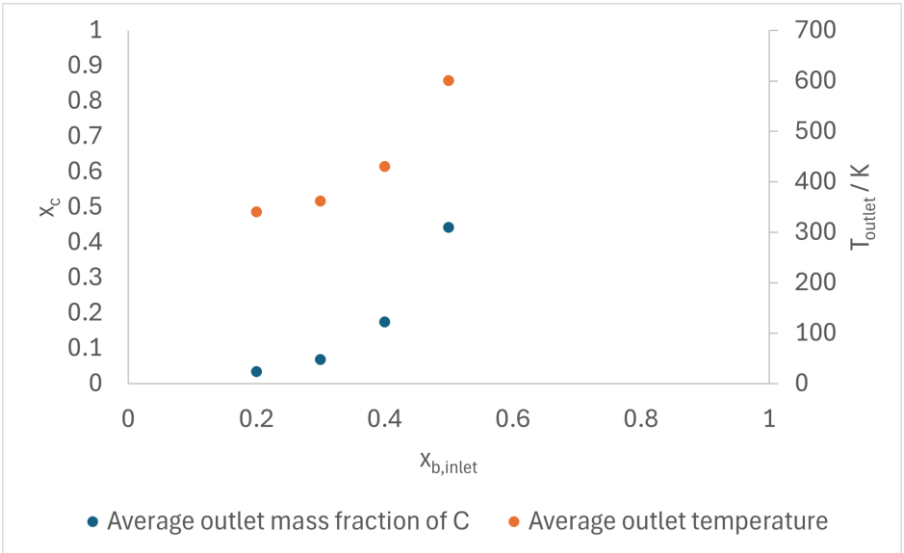

Figure 4-22: x_c and T_{outlet} for different $x_{b,inlet}$ values, $x_{a,inlet}$ = 0.5

As mentioned before, the expected maximum x_c in cases where $x_{a,inlet} = x_{b,inlet}$ is the value of the inlet molar fractions of A and B. However, for the above-mentioned cases there is a limiting species whose fraction varies. This also changes the theoretical maximum x_c, making comparison of the obtained x_c values alone insufficient. To remedy this, table 4-8 shows the calculated conversion for each case, along with inlet composition and outlet variables.
According to reaction stoichiometry and considering that inlet molar fractions are divided by two, due to the presence of two inlets with equal flow rates, conversion is calculated by dividing x_c by $x_{b,inlet}$ (limiting species).

Table 4-8: x_c, T_{outlet} and conversion for different $x_{a,inlet}$ and $x_{b,inlet}$ values, $U_{inlet} = 1.25 \cdot 10^{-1}$ m·s⁻¹

$x_{a,inlet}$	$x_{b,inlet}$	x_c	T_{outlet} / K	Conversion
1	0.3	0.2997	508.6	0.9990
1	0.2	0.1177	393.2	0.5885
0.7	0.4	0.3986	571.0	0.9964
0.7	0.3	0.1847	436.4	0.6155
0.7	0.2	0.0595	356.0	0.2973
0.6	0.4	0.3640	550.3	0.9099
0.6	0.3	0.1084	387.6	0.3615
0.6	0.2	0.0456	347.3	0.2281
0.5	0.5	0.4428	601.1	0.8856
0.5	0.4	0.1752	430.4	0.4381
0.5	0.3	0.0686	362.2	0.2288
0.5	0.2	0.0344	340.2	0.1722

Temperature values are more acceptable for most cases with values below 400 K being quite common for low conversion scenarios, while high conversion cases are still linked to excessively high temperature levels.
Ideally, temperature values should remain below 373 K, which corresponds to 100 ºC, while maintaining levels high enough for conversion to be as high as possible, as this homogeneous reaction would continue after reaching the reactor outlet.

If the reaction was to be faster, by having a larger pre-exponential factor or a lower activation energy, conversion might increase in cases where inlets are more diluted while limiting total heat energy released. Higher conversion could also be achieved by decreasing reactor flow rate, which increases space-time and thus overall production. This also comes with the caveat that low velocities may cause thermal runaways, as was seen in the first subchapter of this parametric study.

Furthermore, reactor geometry can be modified, as was mentioned in the previous subchapter. Reducing reactor diameter while increasing length to maintain a similar space-time would help in cooling the high conversion cases obtained by providing a larger heat transfer surface and reducing reactor-side thermal resistance.

Low conversion cases with T_{outlet} values below 400 K were selected, and inlet velocity was reduced to $6.25 \cdot 10^{-2}$ m·s^{-1}. Table 4-9 shows the obtained results, with non-converging cases marked as "-".

Table 4-9: x_c, T_{outlet} and conversion for different $x_{a,inlet}$ and $x_{b,inlet}$ values, $U_{inlet} = 6.25 \cdot 10^{-2} m \cdot s^{-1}$

$x_{a,inlet}$	$x_{b,inlet}$	x_c	T_{outlet} / K	Original Conversion	Conversion
0.7	0.2	-	-	0.2973	-
0.6	0.3	-	-	0.3615	-
0.6	0.2	0.1319	397.6	0.2281	0.6594
0.5	0.3	0.2779	487.2	0.2288	0.9263
0.5	0.2	0.0908	372.5	0.1722	0.4539

The conversion values obtained increased alongside outlet temperature, as expected. Of the converging cases, the first and third maintained an outlet temperature below 400 K, although maximum temperature remained above 400 K, as seen in the temperature contours shown in figure 4-23.

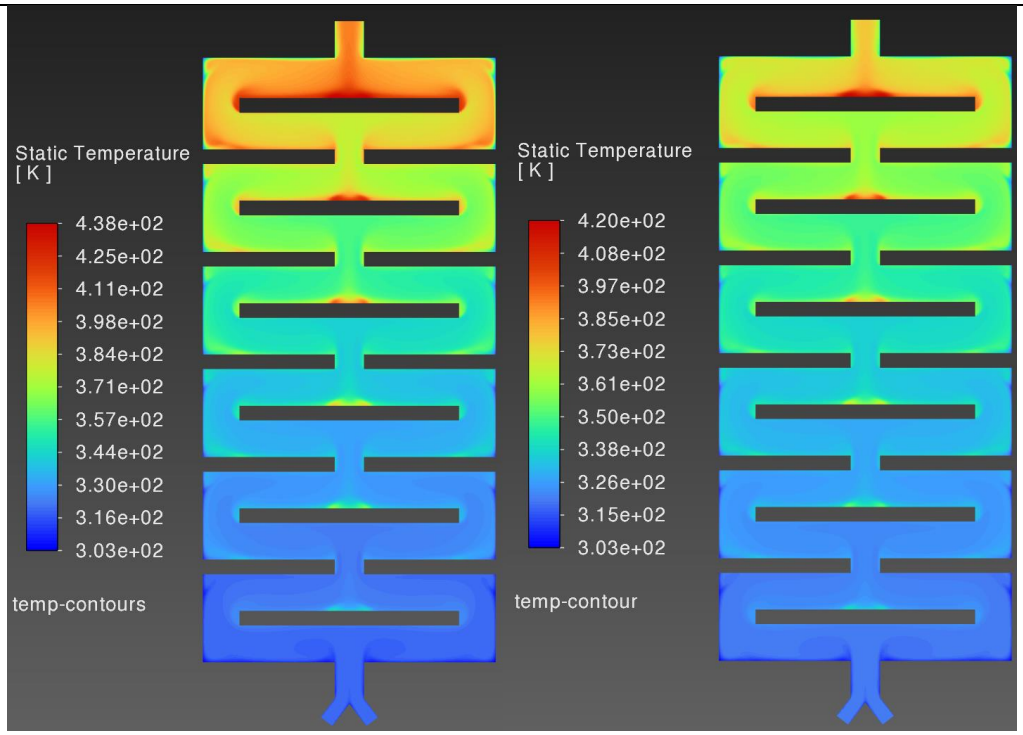

Figure 4-23: Temperature contours for the first and third converging points in table 4-9, respectively.

4.3.6. Reaction parameters

Two cases were selected for testing the influence of E_a values, the lowest temperature cases from subchapter 4.3.4, with $h = 1000W \cdot m^{-2} \cdot K^{-1}$, and subchapter 4.3.5, with $x_{a,inlet} = 0.5, x_{a,inlet} = 0.2$ and $U_{inlet} = 0.0625m \cdot s^{-1}$. The numerical results obtained for the outlet variables are plotted in figures 4-24 and 4-25.

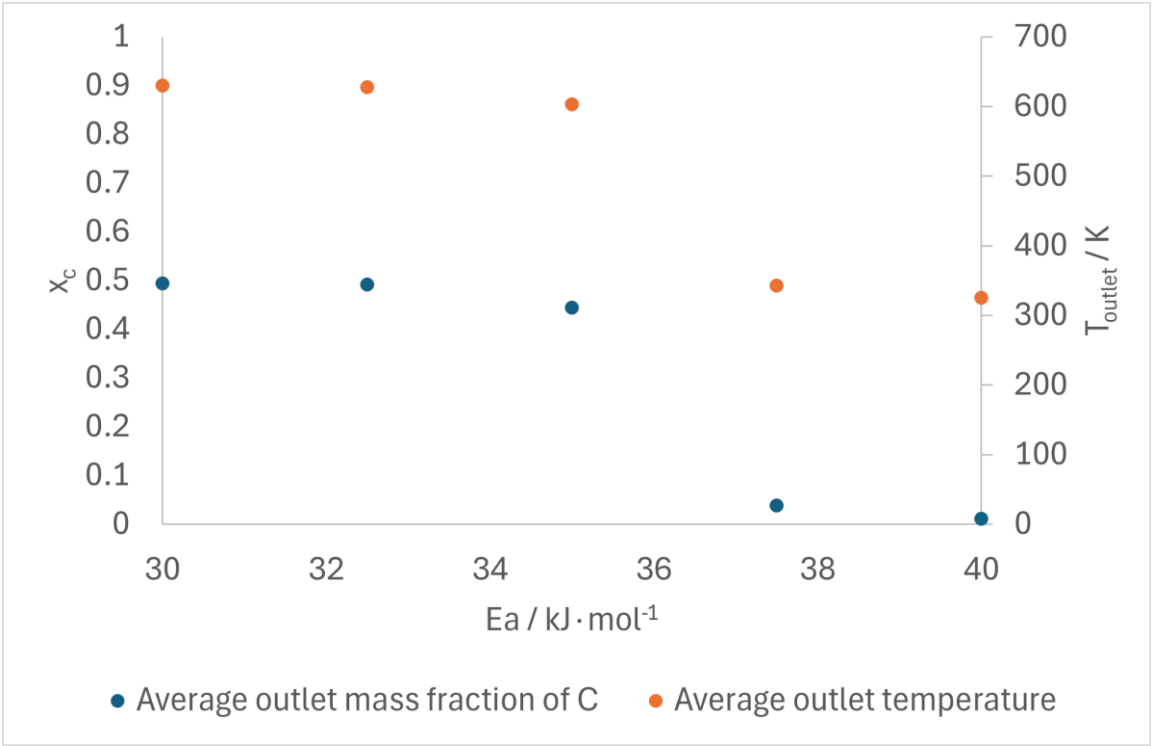

Figure 4-24: x_c and T_{outlet} for different E_a values, $x_{a,inlet} = x_{b,inlet} = 0.5$

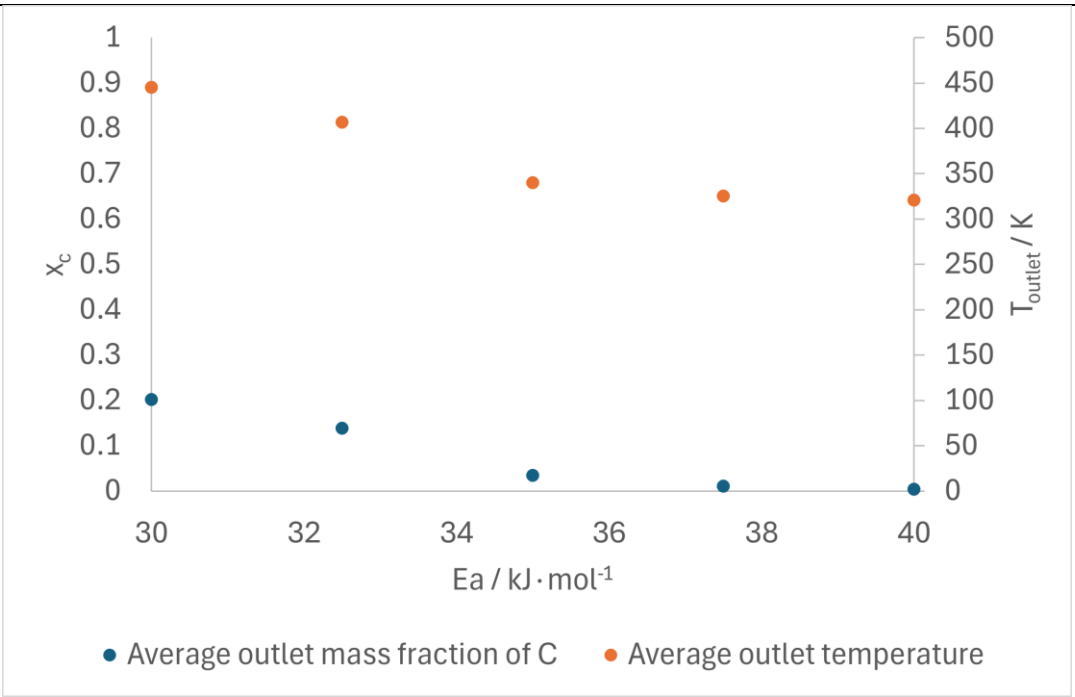

Figure 4-25: x_c and T_{outlet} for different E_a values, $x_{a,inlet}$ = 0.5, $x_{b,inlet}$ = 0.2

For the first case, as E_a decreases from the original value of 35 kJ·mol^{-1}, the outlet variables remain similar. This is due to the almost total conversion of the reactants for cases where $E_a \leq 35kJ \cdot mol^{-1}$, with small increases as conversion becomes complete. On the other hand, as E_a increases there is a sharp drop in outlet temperature and molar fraction of C, likely due to the already observed reaction rate limitation related to low inlet temperature.

In the second case, the same behaviour occurs as E_a decreases, but the rise of x_c and temperature is more gradual. This might be related to an overall lower reaction rate due to lower concentration of species B.

Finally, different values of *ΔH* were tested. As reaction enthalpy increases (absolute value, as it is exothermal), overall heat generation rises, which causes two effects, one directly and the other indirectly.

Directly, fluid temperature increases, which is problematic, since temperatures are already higher than desired in most cases.

Indirectly, reaction rate increases due to the feedback loop between temperature and heat release. As A and B react, heat is released, and reaction rate increases in line with the Arrhenius law as temperature increases. This then results in larger heat energy released as A and B react faster, increasing temperature further and continuing the loop. Higher *ΔH* accelerates this loop even further, as more energy is released by a given quantity of reactant, exacerbating thermal runaways and making non-convergence more common.

As base cases, the systems with $x_{a,inlet} = 0.5, x_{b,inlet} = 0.2$ from the previous section were selected, using U_{inlet} values of $1.25 \cdot 10^{-1}$ and $6.25 \cdot 10^{-2}$ m·s^{-1}. Several *ΔH* values were tested, starting from -50 down to -100 kJ·mol^{-1}, with increments of -5 kJ·mol^{-1}. Non-converging points are excluded from the result plots, shown in figures 4-26 and 4-27.

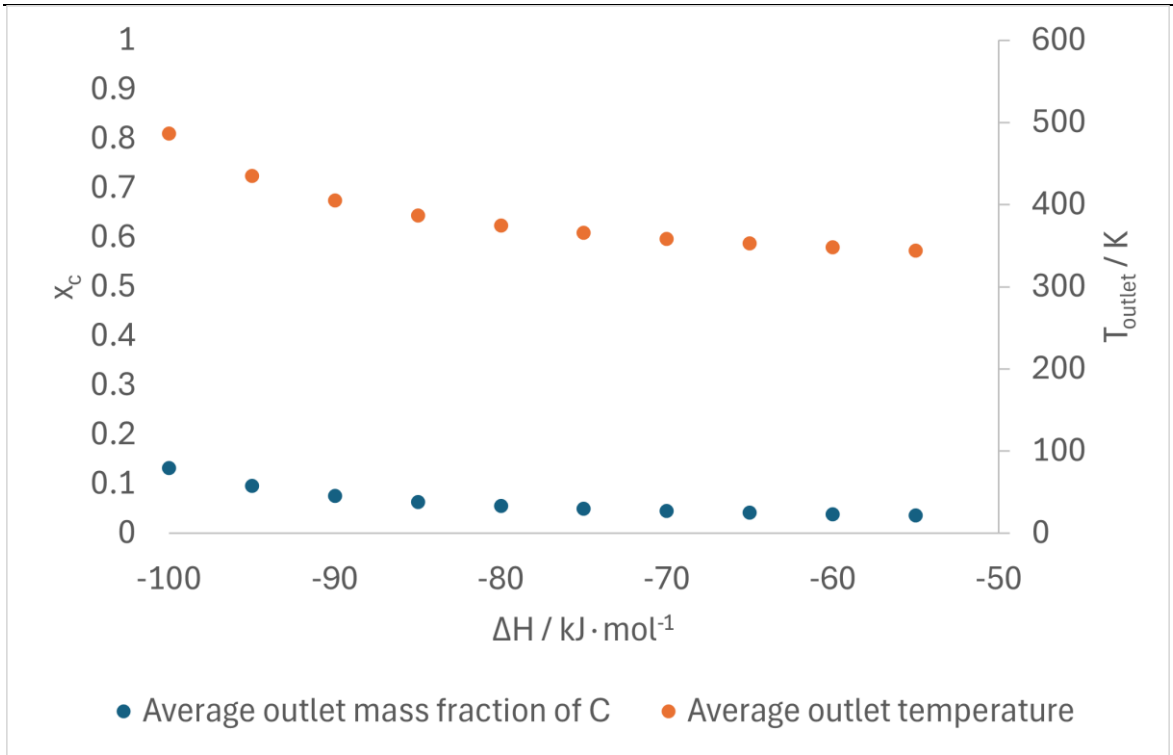

Figure 4-26: x_c and T_{outlet} for different E_a values, $x_{a,inlet}$ = 0.5, $x_{b,inlet}$ = 0.2, U_{inlet} = 0.125 m·s^{-1}

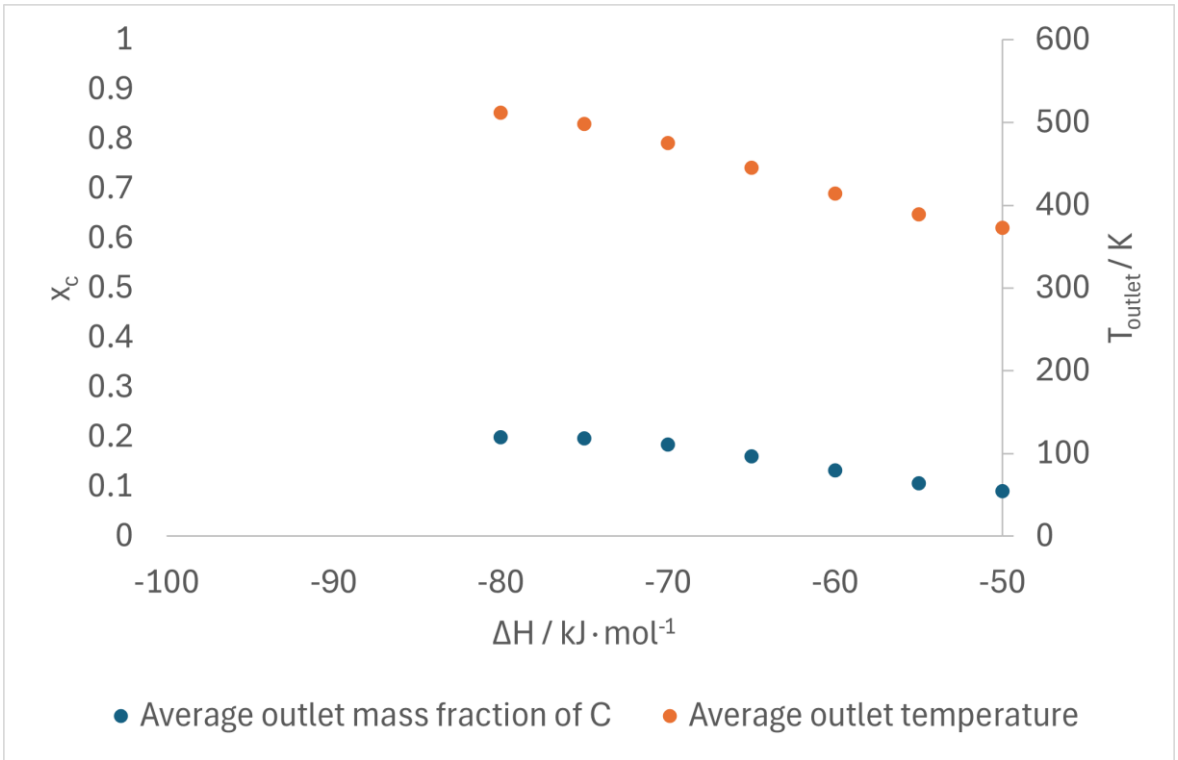

Figure 4-27: x_c and T_{outlet} for different E_a values, $x_{a,inlet}$ = 0.5, $x_{b,inlet}$ = 0.2, U_{inlet} = 0.0625 m·s^{-1}

As mentioned, the increase of *ΔH* leads to both a higher T_{outlet} and a higher x_c. The lower velocity case experienced runaways for $\Delta H \leq -85 kJ \cdot mol^{-1}$ while the higher velocity case remained convergent. Temperature contours of the hottest cases, i.e, those with the highest reaction enthalpy, are shown in figure 4-28.

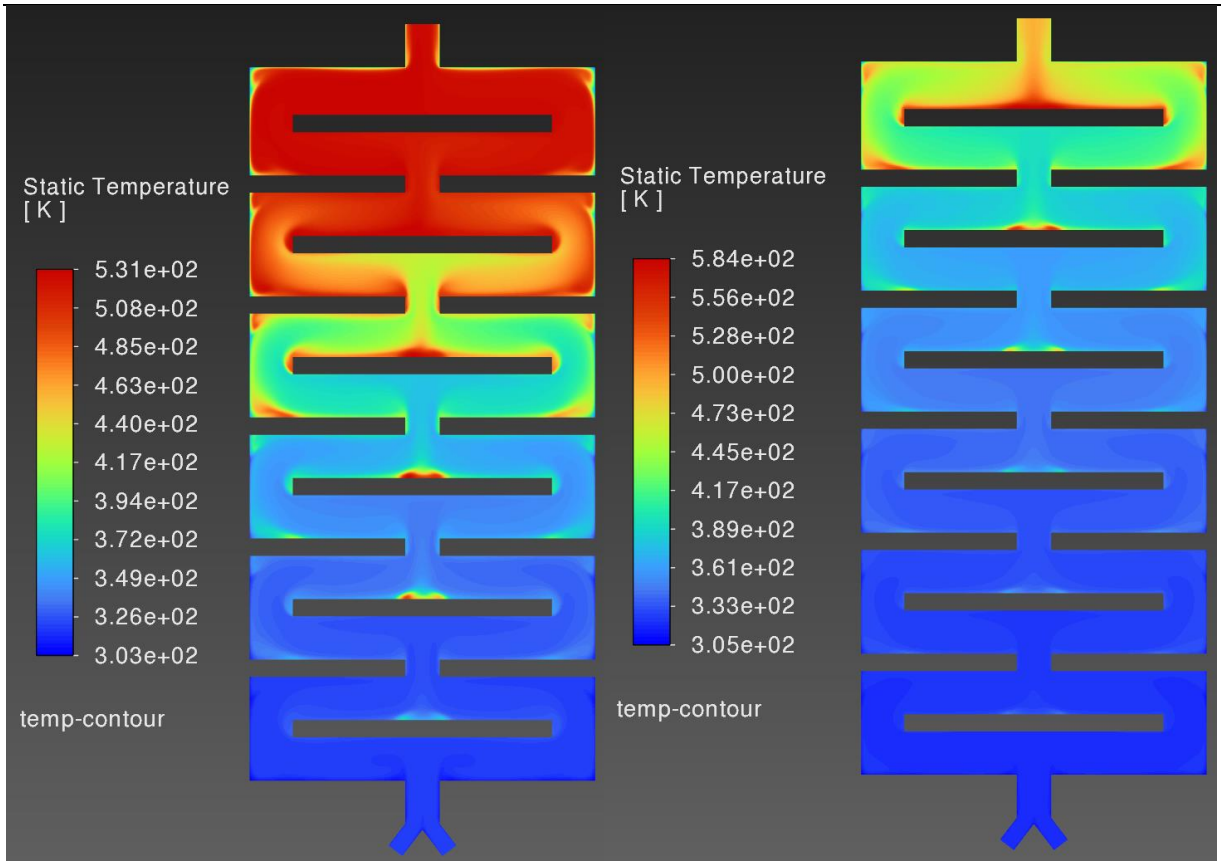

Figure 4-28: Temperature contours for the hottest cases

Lower velocity leads to higher space-time which benefits conversion and thus heat generation, but it also "concentrates" heat in smaller zones due to lower fluid movement, which promotes thermal hotspots.

The surge in heat released leads to temperatures beyond desirable values, and unless reactor input is diluted even further, there is no non-geometric way of tackling the challenge of cooling the reactor, especially its hottest inner zones. Greater *h* values would decrease average outlet temperature, but as was seen in section 4.3.4, this has no significant effect on internal hotspots, making inner section by external cooling alone unfeasible.

5. Conclusions and future perspectives

In this work a sizable parametric study of a hypothetical homogeneous liquid phase reaction was carried out in a non-isothermal system, producing a compilation of numerical data that can be used to guide further study in this topic. To accomplish this, a domain and its corresponding mesh were created, followed by mesh independence testing and tracer predictions, to evaluate reactor hydrodynamics. From here, the parametric study itself was performed, testing the effects of several reaction parameters and system boundary conditions on the outlet variables, the temperature and the molar fraction of the product, species C.

First, the effects of differing Re_{inlet} values were tested, consequently altering the inlet velocity and flow rates. From here, important phenomena were observed, specifically the deviation from expected behaviour as flow rate decreases. As flow rate decreases conversion should steadily increase, due to larger reactor space-time. Instead, a large discrepancy was observed due to the transition from turbulent behaviour to a laminar regime impacting reactant mixing, creating a case with a comparatively high residence time that had low conversion, due to insufficient reagent mixing, while a higher flow rate case experienced a thermal runaway. Following this observation, simulations with no chemical reaction were carried out, feeding A and B to evaluate mixing throughout the system.

Second, the effect of inlet temperature on the outlet variables was evaluated. Here, a comparison was made between a system controlled by mixing and one by the chemical reaction itself. Increasing inlet temperature in the first system did not result in higher conversion, as a higher temperature level leads to higher reaction rates, according to the Arrhenius law, but due to insufficient mixing overall production remains nearly constant. In the second case, 320 K was determined as the minimum inlet temperature required for close to complete reaction, with higher values only increasing outlet temperatures due to adiabatic operation.

Third, heat transfer to the outside of the reactor was added, using a convective outer medium, kept at a constant temperature of 300 K. The main conclusion of this part of the study was that while heat transfer through reactor walls decreased average outlet temperatures, reactor hotspots remained largely unaffected, showing that heat transfer to the outside of the reactor alone is insufficient, highlighting the need for internal cooling elements.

Fourth, inlet reactant molar fractions were also changed. Diluted inlets directly contribute to lower reaction rates, which slow down heat release, but also limit the total potential heat energy released due to lower reagent quantity. Although temperature levels remained closer to more acceptable temperature levels while still maintaining appreciable conversion, hotspot temperatures remained unrealistic.

The final part of the study tested the effect of reaction activation energy and enthalpy, concluding that higher enthalpy values intensify the feedback loop between temperature and heat released due to chemical reaction, which exacerbates temperature values and reaction rates, leading to thermal runaway.

Regarding technical aspects of the work, the created methodology allowed for almost completely automatic simulations, including the automatic definition of reaction parameters, which was not used in previous works. This portion of the methodology should allow for easier exploration of reaction parameters in future works, accelerating the simulation process. Without it, the user would instead have to manually change variables in Fluent®, tedious and time-consuming.

A few limitations of the created methodology were also identified. Specifically, due to the sensitivity of highly exothermic reactions, non-convergence was obtained in several cases. This is unsatisfactory not only because no useful numerical results are produced, but also because non-converging simulations reach the maximum defined iterations, wasting computational time. Individually, this time loss is negligible, but over time and over hundreds of simulations this wasted time adds up. Furthermore, more time is needed for data interpretation and organisation, as non-converging cases need to be identified, as they may have stopped at a time where recorded variables seem plausible. A potential fix is using a stricter maximum number of iterations, but this might be impossible while studying a wide range of parameters, which might require a wildly different number of total iterations to compute.

Regardless, the inherent limitations of the methodology do not outweigh the advantages, as the time saved due to almost complete automation surpasses the time loss due to non-convergence, which is only especially relevant due to the sensitivity of the studied system and can potentially be fixed, removing this source of inefficiency.

This work also presents an initial starting point for research, use and validation of turbulence models in the host research group. Focusing on cooling, whether by adding internal elements in a counter-current arrangement or using geometric alterations to reduce reactor-side resistance, is an avenue for future work which should help control reactor temperatures, increasing the potential range of suitable reaction parameters while maintaining high conversion levels. Finally, using a non-hypothetical homogeneous reaction with parameters similar to the reaction used in the parametric study should open the way for further validation. The previous thesis done on this topic validated the hydrodynamic behaviour of the performed simulations by comparing tracer CFD predictions to tracer experiments done in a resin 3D printed reactor. Repeating this idea by comparing the performance of the simulated reactor to an experimental installation or at the least a known reaction, could further validate this design method for this use case.

6. Assessment of the work performed

6.1. Accomplished Objectives

As defined in the introduction, this work successfully created a large set of numerical data used to evaluate the effect of different parameters and boundary conditions in the performance of an illustrative reaction system. Additionally, several limitations were identified, both in regards to the selected reactor design and methodology.

6.2. Contribution to the Sustainable Development Goals

SGD 8 (Decent Work and Economic Growth) focuses on promoting sustainable economic growth, alongside productive employment and decent work for all.
SGD 9 (Industry, Innovation and Infrastructure) revolves around the construction of quality and reliable infrastructure, sustainable industrialization and the promotion of innovation.

Table 6-1: Contributions to the Sustainable Development Goals

SDG	Target	Contribution	Indicators of performance and metrics
8	2	This work explores the systematic improvement of existing processes by providing a framework for optimization.	Increased process performance via optimization.
9	4	This work provides a workflow that can be used for prototyping, evaluation and optimization of new, greener and more efficient chemical processes.	Allows for faster development of new, greener and more optimized processes.

6.3. Final assessment

This project proved to be equally rewarding as it was frustrating at times. CFD is an exceptionally powerful tool for reactor design and study, which is further simplified by the tools produced by ANSYS, allowing for ease of use and automation. Of course, ease of use does not equal simplicity, and research is still required to both prepare and to interpret the performed simulations.
The main sources of frustration stem from some seemingly arbitrary limitations from Fluent, such as the impossibility of defining material properties and reaction parameters as input parameters, requiring the use of the TUI system. Furthermore, highly exothermic reactions proved to be incredibly sensitive, with cases with no production being separated from thermal runaway cases by a few degrees of difference in inlet temperature. This resulted in a large amount of time spent in fine tuning the initial parameters for the study.
Still, despite some frustration and despite the excessive times required for some simulations (on average, tracer predictions required 20 hours of continuous simulation), this work was

incredibly rewarding, greatly expanding my knowledge of CFD and the ANSYS CFD suite. This is especially true with regards to automation and turbulence models, where I learned several important limitations and settings.

7. References

[1] Cañas, Héctor, Josefa Mula, Manuel Díaz-Madroñero, and Francisco Campuzano-Bolarín. 'Implementing Industry 4.0 Principles'. *Computers & Industrial Engineering* 158 (August 2021): 107379. https://doi.org/10.1016/j.cie.2021.107379.

[2] Ansari, A., Mohaghegh, S., Shahnam, M., Dietiker, J. F., Takbiri Borujeni, A., Fathi, E., "Data Driven Smart Proxy for CFD: Application of Big Data Analytics & Machine Learning in Computational Fluid Dynamics, Part One: Proof of Concept"; NETL-PUB-21574; NETL Technical Report Series; U.S. Department of Energy, National Energy Technology Laboratory: Morgantown, WV, 2017.

[3] Porter, Chris, and Niveditha Krishnamoorthy. 2022. "The Computational Fluid Dynamics Revolution Driven by GPU Acceleration." *NVIDIA Developer Blog*, May 26, 2022.

[4] Fletcher, David F. 'The Future of Computational Fluid Dynamics (CFD) Simulation in the Chemical Process Industries'. *Chemical Engineering Research and Design* 187 (November 2022): 299–305. https://doi.org/10.1016/j.cherd.2022.09.021.

[5] Soto, Victor, Claudia Ulloa, and Ximena Garcia. 'A CFD Design Approach for Industrial Size Tubular Reactors for SNG Production from Biogas (CO2 Methanation)'. *Energies* 14, no. 19 (2021): 6175. https://doi.org/10.3390/en14196175.

[6] *ANSYS, Inc. Fluent® Theory Guide*. Release 2024 R2. ANSYS, Inc., 2024. https://ansyshelp.ansys.com/public//////Views/Secured/corp/v242/en/flu_th/flu_th.html (accessed in 2025).

[7] Hirsch, Charles. *Numerical Computation of Internal and External Flows: The Fundamentals of Computational Fluid Dynamics* 2nd ed. Butterworth–Heinemann, 2007.

[8] *ANSYS, Inc. Fluent® User's Guide*. Release 2024 R2. ANSYS, Inc., 2024. https://ansyshelp.ansys.com/public//////Views/Secured/corp/v242/en/flu_ug/flu_ug.html (accessed in 2025).

[9] Moon, Jiyoung, Dela Quarme Gbadago, and Sungwon Hwang. '3-D Multi-Tubular Reactor Model Development for the Oxidative Dehydrogenation of Butene to 1,3-Butadiene'. *ChemEngineering* 4, no. 3 (2020): 46. https://doi.org/10.3390/chemengineering4030046.

[10] Wehinger, Gregor D., Matteo Ambrosetti, Raffaele Cheula, et al. 'Quo Vadis Multiscale Modeling in Reaction Engineering? – A Perspective'. *Chemical Engineering Research and Design* 184 (August 2022): 39–58. https://doi.org/10.1016/j.cherd.2022.05.030.

[11] Levenspiel, Octave. *Chemical Reaction Engineering. Hauptbd.* 3. ed. Wiley, 1999.

[12] A.E. Rodrigues, "Theory of Residence Time Distributions", *Multiphase Chemical Reactors*, A.E. Rodrigues, J.M. Calo e N.H. Sweed (Eds.), NATO ASI Series, Sijthoff Noordhoff, No. 51, Vol. I, 225 (1981).

[13] A. Monteiro, "CFD application in parametric studies of non-isothermal reactors", Master's diss., (University of Porto, 2024)

Annex A – Sustainable Development Goals

Figure Annex A-1: Logos of the SDGs applied to this work

Appendix A – Reactor geometry dimensions

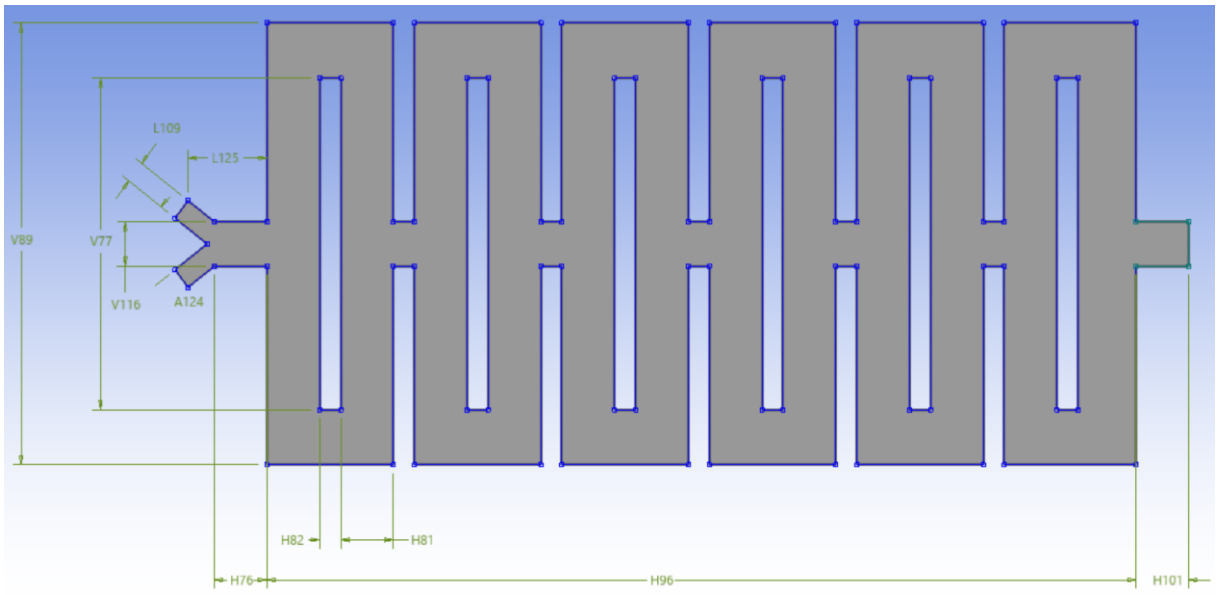

Figure Appendix A-1: Reactor geometry sketch for the two inlet case

In addition to the dimensions shown in table 12, several constraints were used to ensure vertical symmetry and equal lengths. For example, an equal length constraint is applied to the inlets so that both have the same length, even though only one has a dimension applied.

Table Appendix A-1: Dimensions for the two inlet sketch

	Dimension
A124	75°
H101	1 cm
H76	1 cm
H81	1 cm
H82	0.4 cm
H96	16.5 cm
L109	0.4 cm
V116	0.8 cm
V77	6 cm
V89	8 cm

The following geometry was used in a preliminary parametric study, using different values from those used in the study in the main body of this work.

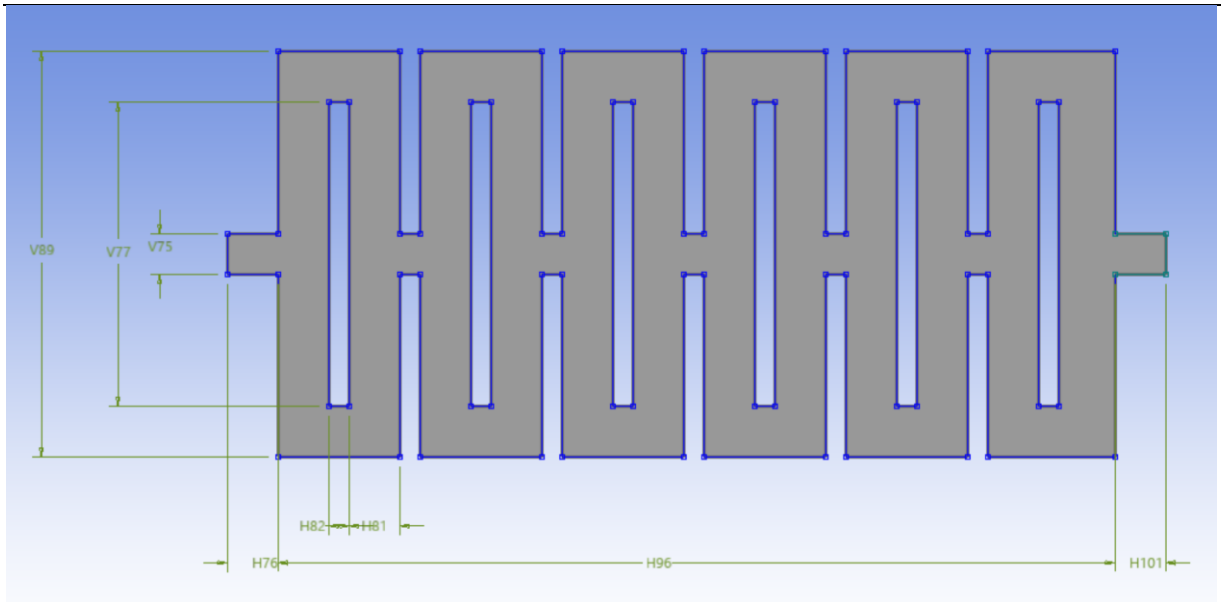

Figure Appendix A-2: Reactor geometry for a single inlet

Table Appendix A-2: Dimensions for single inlet sketch used in simulations of Appendix B

	Dimension
H101	1 cm
H76	1 cm
H81	1 cm
H82	0.4 cm
H96	16.5 cm
V75	0.8 cm
V77	6 cm
V89	8 cm

Appendix B – Preliminary parametric study

The parametric study presented in this appendix was done before the one presented in the main work, using reference values present in a previous work done on this dissertation topic. Exploring these values (k_0, E_a and *ΔH*) in the current reactor design resulted in unrealistic cases regarding the temperature values obtained. This led to the necessity of a new expanding the study to a new range of parameters' values that produced more realistic temperature outputs, which is in the main body of this work. Besides the search for more mild temperature values, initially, a reactor with one inlet was also considered instead of the one with two inlets reported in the previous chapters. As such, a comparison between the two inlet configurations was done, to verify the effect of assuming perfectly mixed reagents fed to the reactor.

a. Inlet velocity and reaction enthalpy

The first study revolves around the variation of U_{inlet}, and consequently flow rate, for different *ΔH* values. The used values for velocity were {0.25, 0.1875, 0.125, 0.0625, 0.0125} m·s^{-1}. The remaining parameters are detailed in table B-1, and the obtained x_c and T_{outlet} are shown in figures B-1 and B-2.

Table Appendix B-1: Reaction parameters and boundary conditions for inlet velocity study.

k_0 / m^3·kmol^{-1}s^{-1}	Ea / kJ ·mol^{-1}	T_{inlet} / K	$x_{a,inlet}$	$x_{b,inlet}$	h / W·m^{-2}K^{-1}	$T_{outside}$ / K
1	50	400	0.5	0.5	0	400

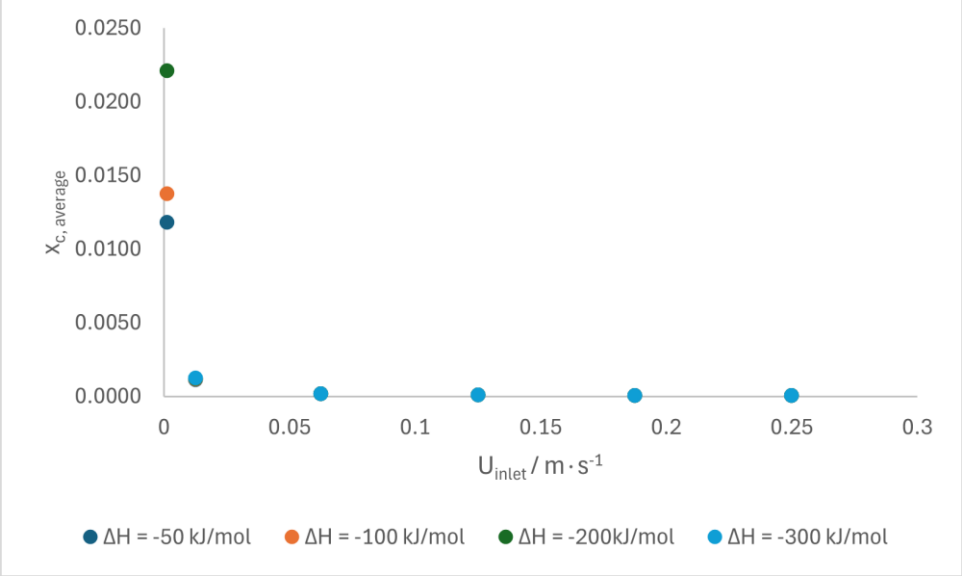

Figure Appendix B-1: x_c, for each velocity and enthalpy.

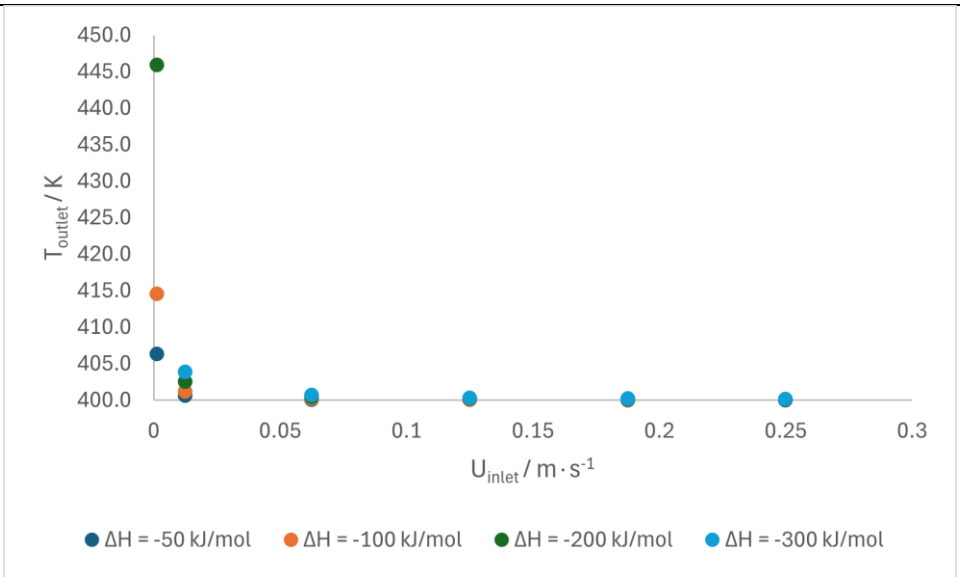

Figure Appendix B-2: T_{outlet}, for each velocity and enthalpy.

Unlike the cases presented in the main body, for these reaction parameters, inlet velocity variation was unable to produce cases with significant conversions. The observed behaviour due to sufficient mixing alongside low residence times remains absent as well, due to reactants being perfectly mixed at the singular reactor inlet. Thermal runaways occurred for $\Delta H = -300\ kJ \cdot mol^{-1}$, at the lowest velocity.

b. Convection coefficient and outside temperature

External heat transfer was studied using *h* and $T_{outside}$ values of {0, 50, 100, 250, 500, 1000} W·m^{-2}K^{-1} and {400, 425} K, respectively.

Using the parameters shown in table B-2, average outlet parameters are shown in figures B-3 and B-4.

Table Appendix B-2: Reaction parameters and boundary conditions for heat transfer study.

k_0 / m^3·kmol^{-1}s^{-1}	U_{inlet} / m·s^{-1}	Ea / kJ ·mol^{-1}	T_{inlet} / K	$x_{a,inlet}$	$x_{b,inlet}$
1	0.00125	50	400	0.5	0.5

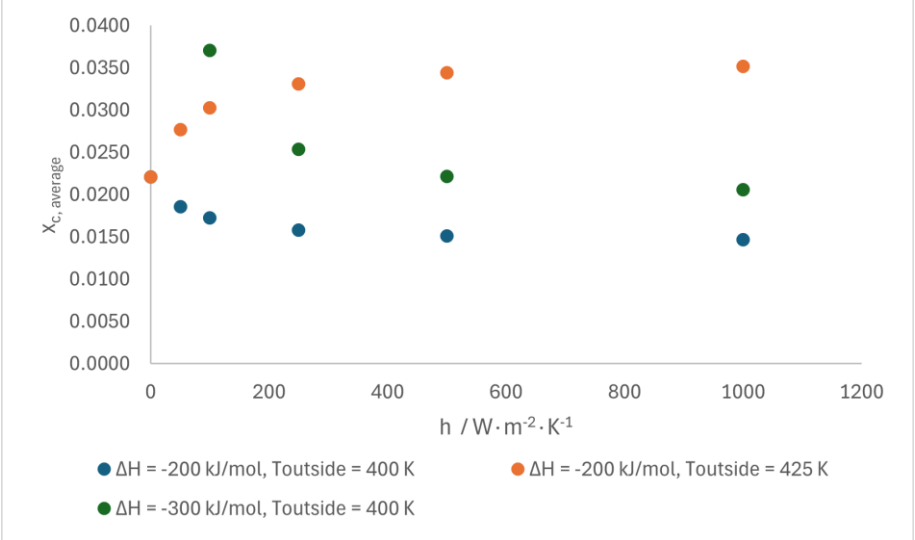

Figure Appendix B-3: x_c, for different values of h and $T_{outside}$, for a given ΔH.

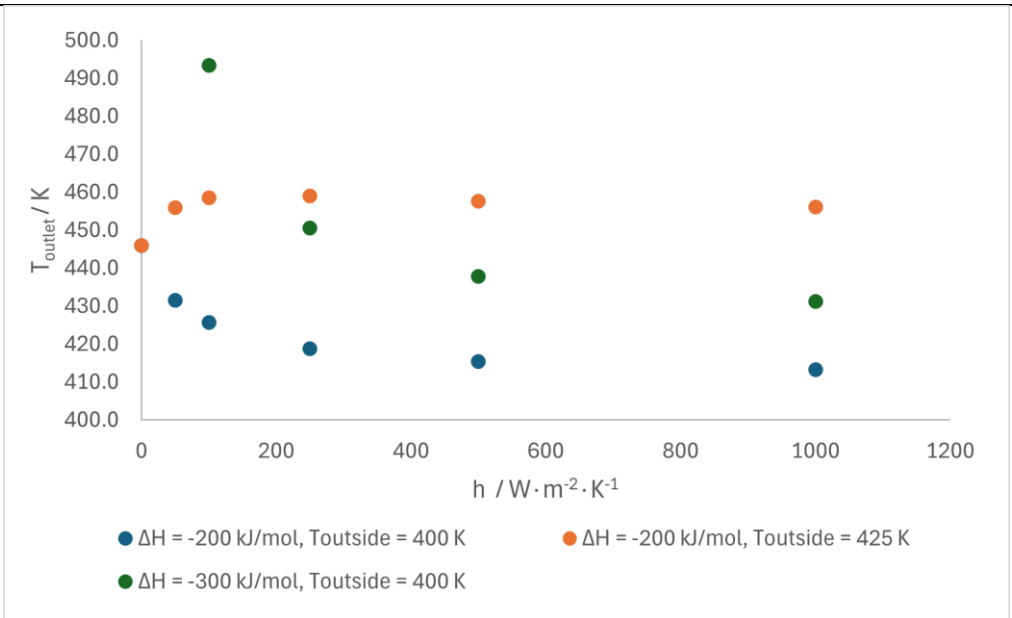

Figure Appendix B-4: T_{outlet}, for different values of h and $T_{outside}$, for a given ΔH.

In accordance with the main study, adding heat transfer reduces outlet temperatures while maintaining similar conversion levels, while leaving reactor hotspots unaffected, as seen on figure B-5.

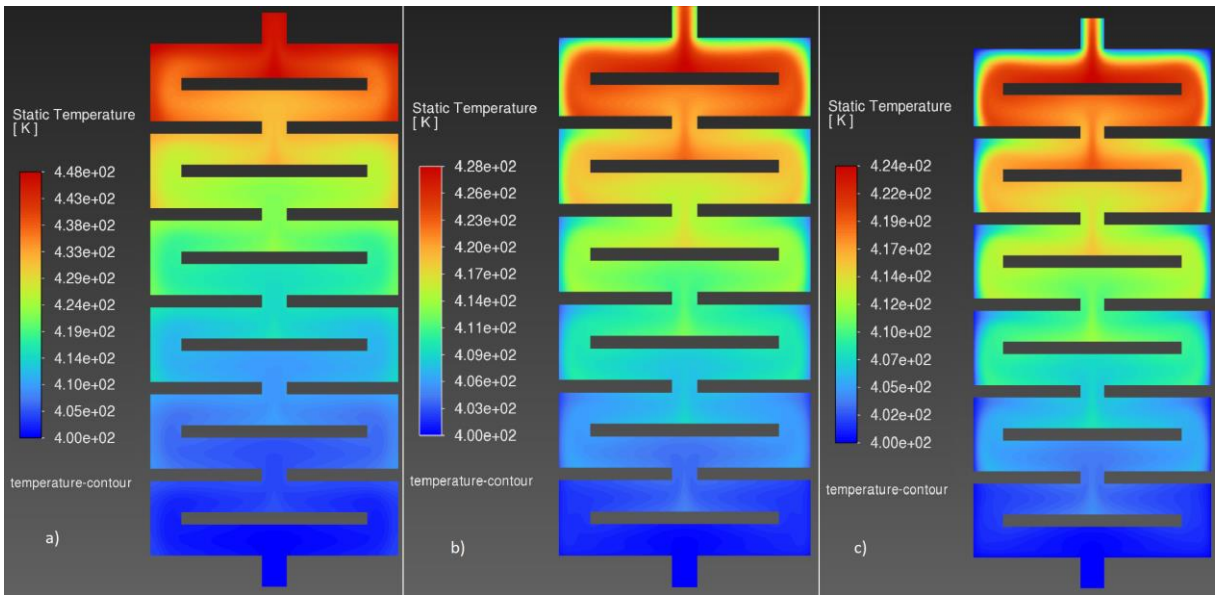

Figure Appendix B-0-5: Temperature contours for ΔH = -200 kJ·mol^{-1}, $T_{outside}$ = 400 K: a) h = 0 W·m^{-2}K^{-1}; b) h = 250 W·m^{-2}K^{-1}; and c) h = 1000 W·m^{-2}K^{-1}.

c. Inlet temperature and heat transfer

Using the parameters shown in table B-3, the effect of varying T_{inlet} was studied, for different values of *h*, with the resulting graphs shown in figures B-6 and B-7.

Table Appendix B-3: Reaction parameters and boundary conditions used for the T_{inlet} study

k_0 / m^3·kmol^{-1}s^{-1}	Ea / kJ ·mol^{-1}	ΔH / kJ·mol^{-1}	$x_{a,inlet}$	$x_{b,inlet}$	$T_{outside}$ / K
1	50	-200	0.5	0.5	600

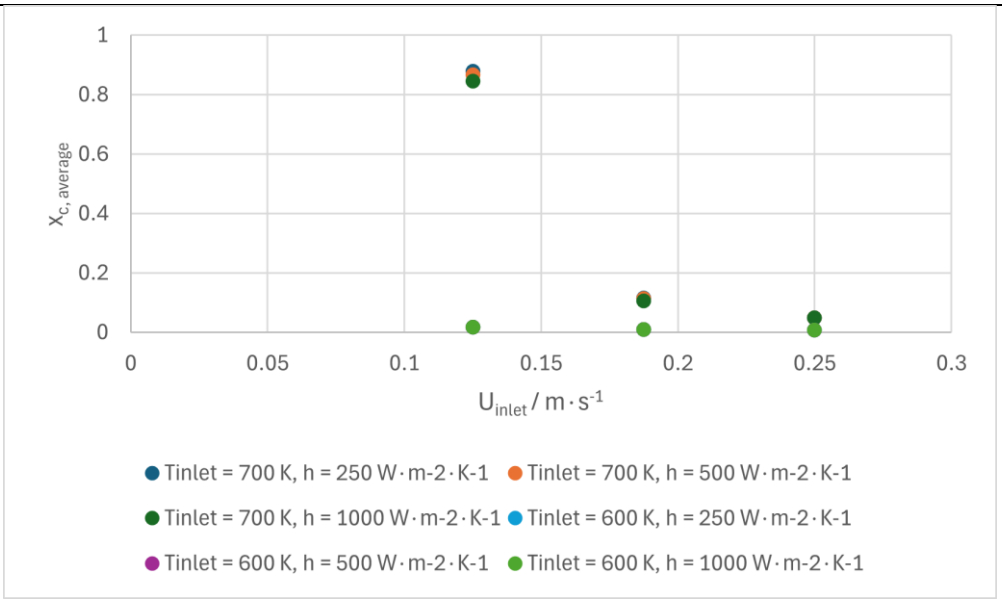

Figure Appendix B-6: x_c, for different values of T_{inlet} and h

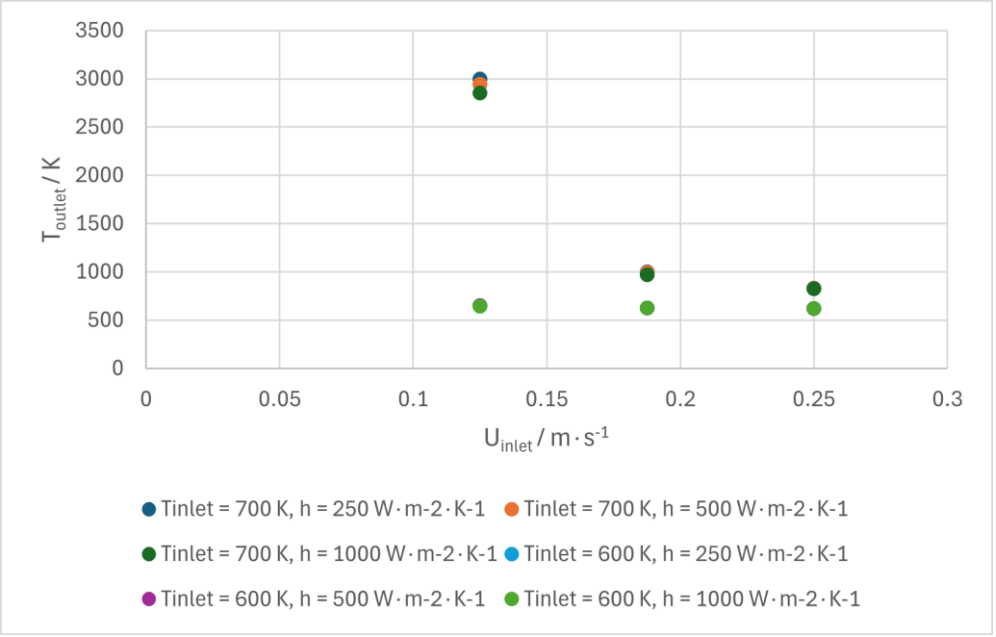

Figure Appendix B-7: T_{outlet}, for different values of T_{inlet} and h.

The obtained results follow the same inlet temperature limitation seen in the main study, where a sufficiently high temperature level leads to full conversion. Of course, due to the higher enthalpy and inlet molar fraction values used, the obtained temperatures are much higher.

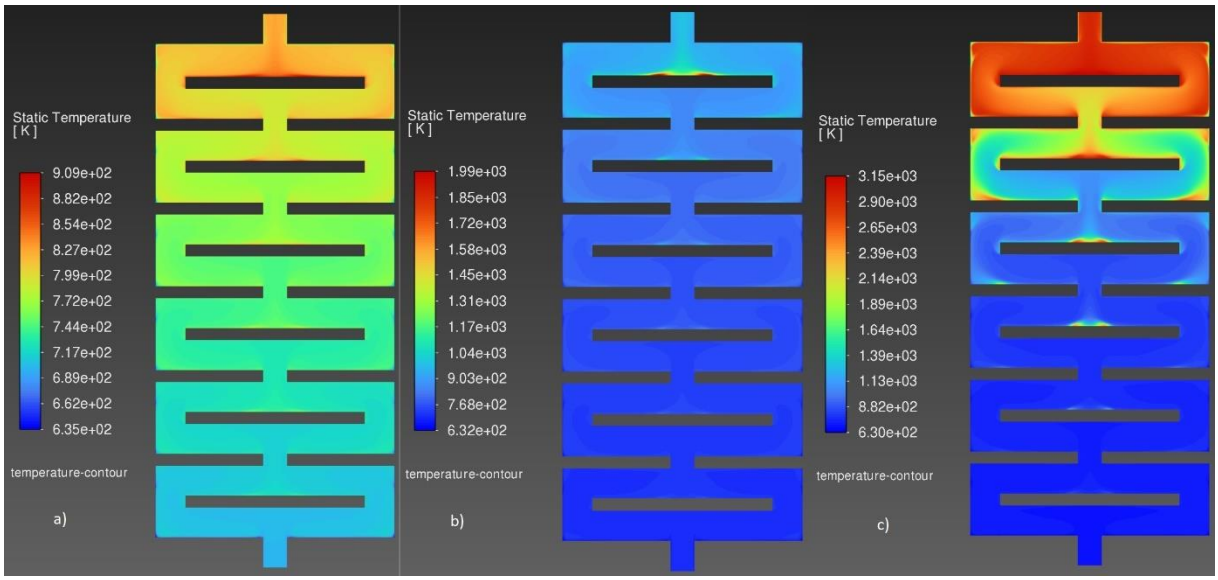

Figure Appendix B-8: Temperature contours for T_{inlet} = 700 K, h = 1000 W·m^{-2}K^{-1}: a) U_{inlet} = 0.25 m·s^{-1}; b) U_{inlet} = 0.1875 m·s^{-1}; c) U_{inlet} = 0.125 m·s^{-1}

d. Inlet molar fractions

Inlet molar fractions, $x_{a,inlet}$ and $x_{b,inlet}$, were tested in the two configurations used in the main work (stoichiometrically; reactant in excess). The U_{inlet} = {0.1875, 0.125} m·s^{-1} and *h* = {500, 1000} W·m^{-2}K^{-1} cases from the Appendix B T_{inlet} study were used as base cases, included in the obtained results, figures B-9 and B-10, to compare to cases with lower inlet molar fractions, with the remaining parameters shown in table B-4.

Table Appendix B-4: Reaction parameters and boundary conditions used for the $x_{a,inlet}$ and $x_{b,inlet}$ study

k_0 / m^3·kmol^{-1}s^{-1}	Ea / kJ ·mol^{-1}	ΔH / kJ·mol^{-1}	T_{inlet} / K	$T_{outside}$ / K
1	50	-200	700	600

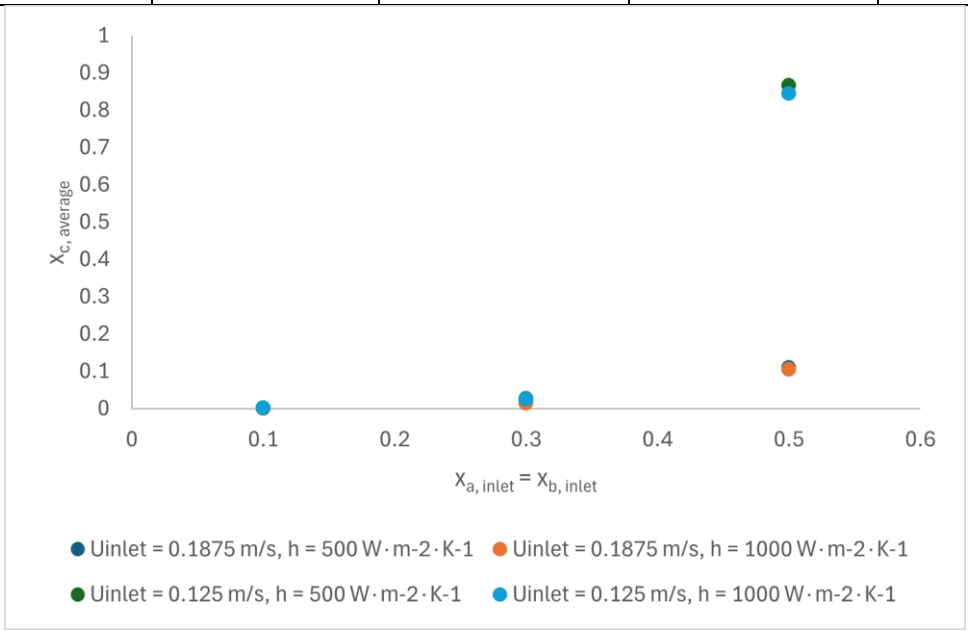

Figure Appendix B-9: x_c, for different values of U_{inlet} and h, while $x_{a,inlet}$ = $x_{b,inlet}$.

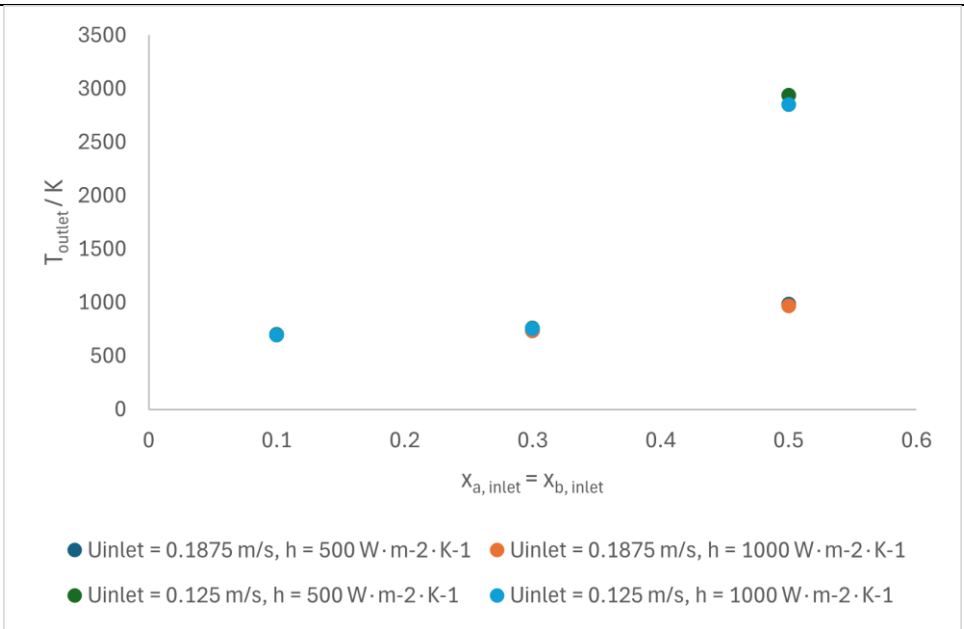

Figure Appendix B-10: T_{outlet}, for different values of U_{inlet} and h, while $x_{a,inlet} = x_{b,inlet}$.

Cases with a reagent in excess, species A, are shown in figures B-11 and B-12, showing a more gradual descent of the output variables, as the theoretical maximum production of C and the overall heat released are decreased by the limited reactant.

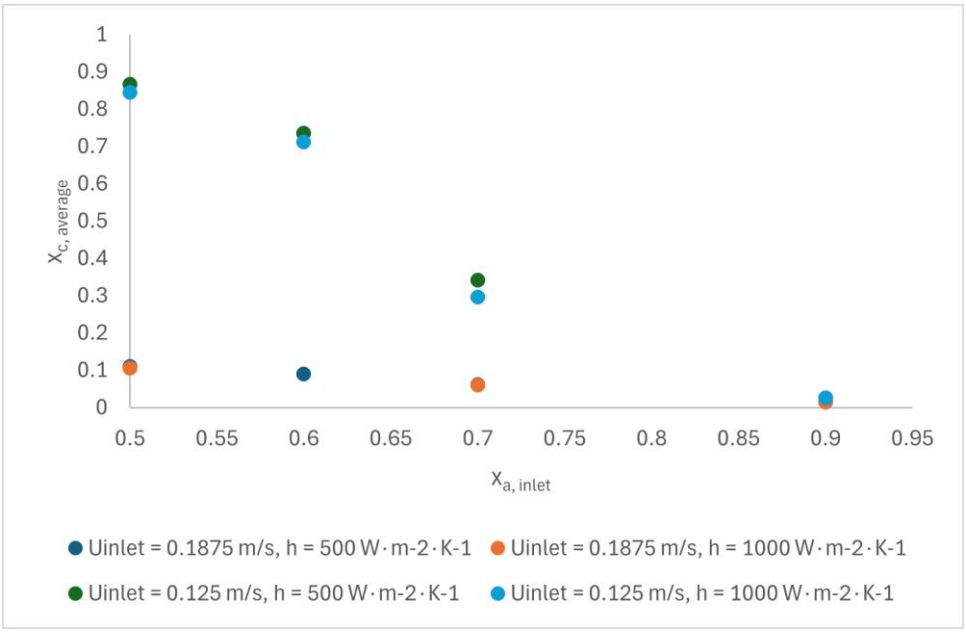

Figure Appendix B-11: x_c, for different values of U_{inlet} and h, while $x_{b,inlet} = 1 - x_{a,inlet}$.

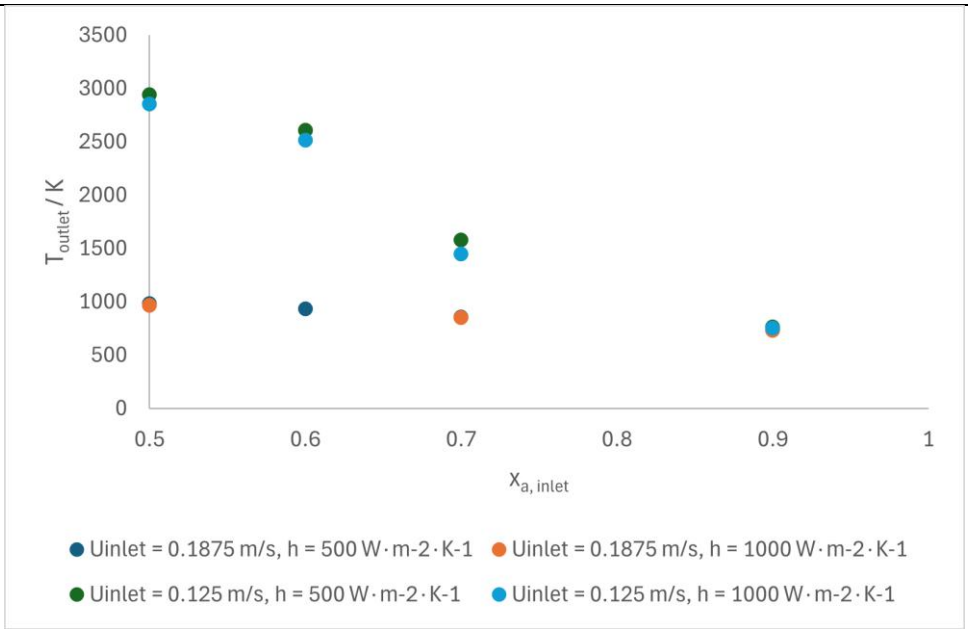

Figure Appendix B-12: T_{outlet}, for different values of U_{inlet} and h, while $x_{b,inlet}$ = 1 - $x_{a,inlet}$.

e. Reaction parameters

The following reaction parameters were chosen: for k_0 = 1 m³·kmol⁻¹·s⁻¹, E_a = {45, 47.5, 50, 52.5, 55} kJ·mol⁻¹ and T_{inlet} = 700 K; for k_0 = 0.1 m³·kmol⁻¹·s⁻¹, E_a = {35, 37.5, 40, 42.5, 45, 47.5, 50} kJ·mol⁻¹ and T_{inlet} = {700, 800} K; for k_0 = 10 m³·kmol⁻¹·s⁻¹, E_a = {50, 52.5, 55, 57.5, 60, 62.5, 65} kJ·mol⁻¹ and T_{inlet} = {600, 700} K. The remaining parameters are shown in table B-5.

Table Appendix B-5: Reaction parameters and boundary conditions used for the E_a and k_0 study

U_{inlet} / m·s⁻¹	ΔH / kJ·mol⁻¹	$x_{a,inlet}$	$x_{b,inlet}$	h / W·m⁻²K⁻¹	$T_{outside}$ / K
0.125	-200	0.5	0.5	500	600

The obtained results are shown in figures B-13 and B-14, except for cases that resulted in thermal runaway. Decreasing E_a while increasing k_0 results in extreme sensitivity to temperature, with either no significant reaction or runaways. Increasing E_a while reducing k_0 did reduce reaction sensitivity, with a gradually decreasing level of x_c and T_{outlet} as E_a increased, which can be compared to the k_0 = 1 m³·kmol⁻¹·s⁻¹ cases where a steep drop-off can be observed from E_a = 50 kJ·mol⁻¹ to 52.5 kJ·mol⁻¹.

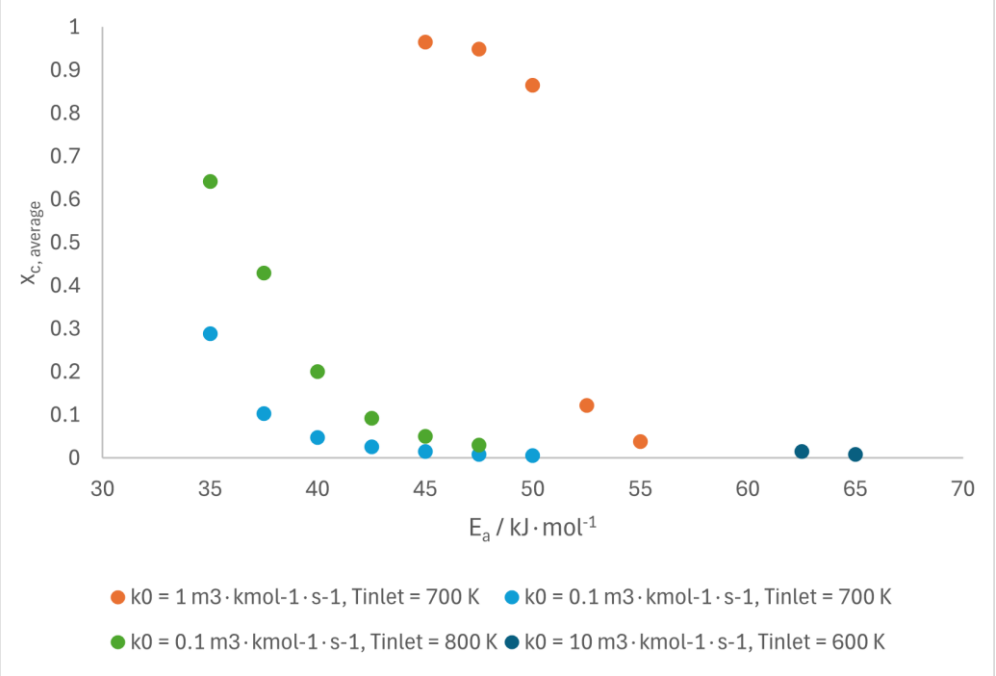

Figure Appendix B-13: x_c, for different values of E_a, for a given k_0 and T_{inlet}.

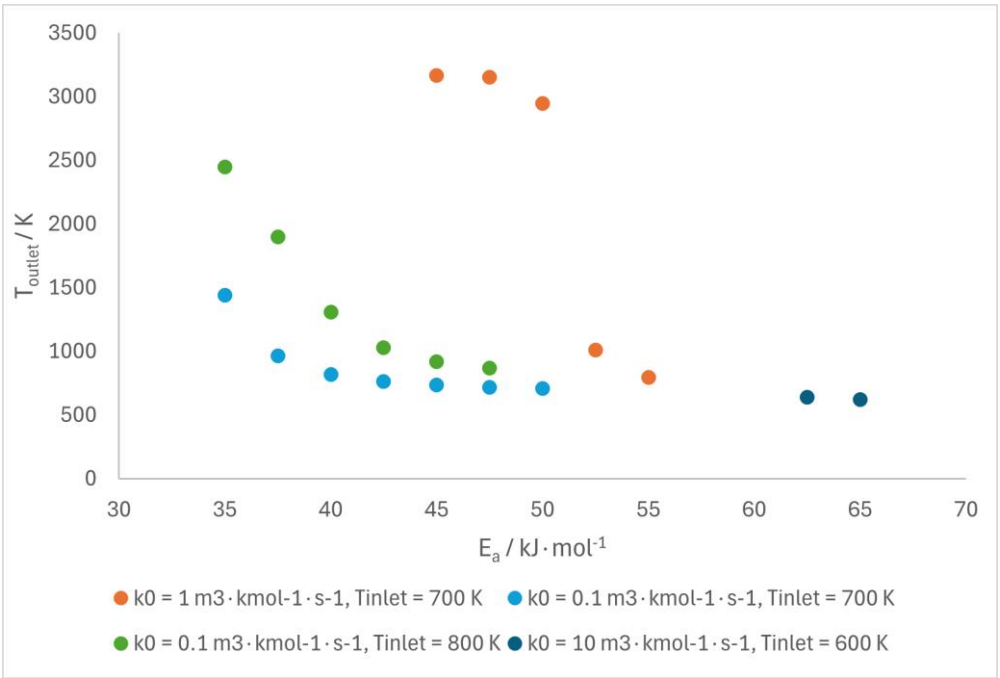

Figure Appendix B-14: T_{outlet}, for different values of E_a, for a given k_0 and T_{inlet}

Temperatures remain high for cases that experience any production of C, due to high reaction enthalpy values.

f. Two inlets

As mentioned, simulations in this appendix use the assumption that reactants enter the reactor pre-mixed, which ignores reactant mixing in the reactor volume. Using the two inlet reactor geometry, the effects of this assumption were tested.

The following case from the appendix B T_{inlet} study was used as comparison between the two geometries: U_{inlet} = 0.125 m·s^{-1}, T_{inlet} = 700 K, h = 500 W·m^{-2}K^{-1}. A comparison between average outlet variables and maximum temperature is shown in table B-5.

Table Appendix B-5: Output parameters for each geometry, for the same case

	x_c	T_{outlet} / K	T_{max} / K
Single Inlet	0.879	2998	3191
Double Inlet	0.819	2844	3154

Reactant mixing was evaluated in a similar manner to the main work, with chemical reaction being disabled in Fluent. The obtained values for this velocity remain similar, as the reactants mix sufficiently. As velocity decreases the disparity between the perfectly mixed case and the non-assumption case would increase, as can be seen in the mass fraction contours shown in figure B-15.

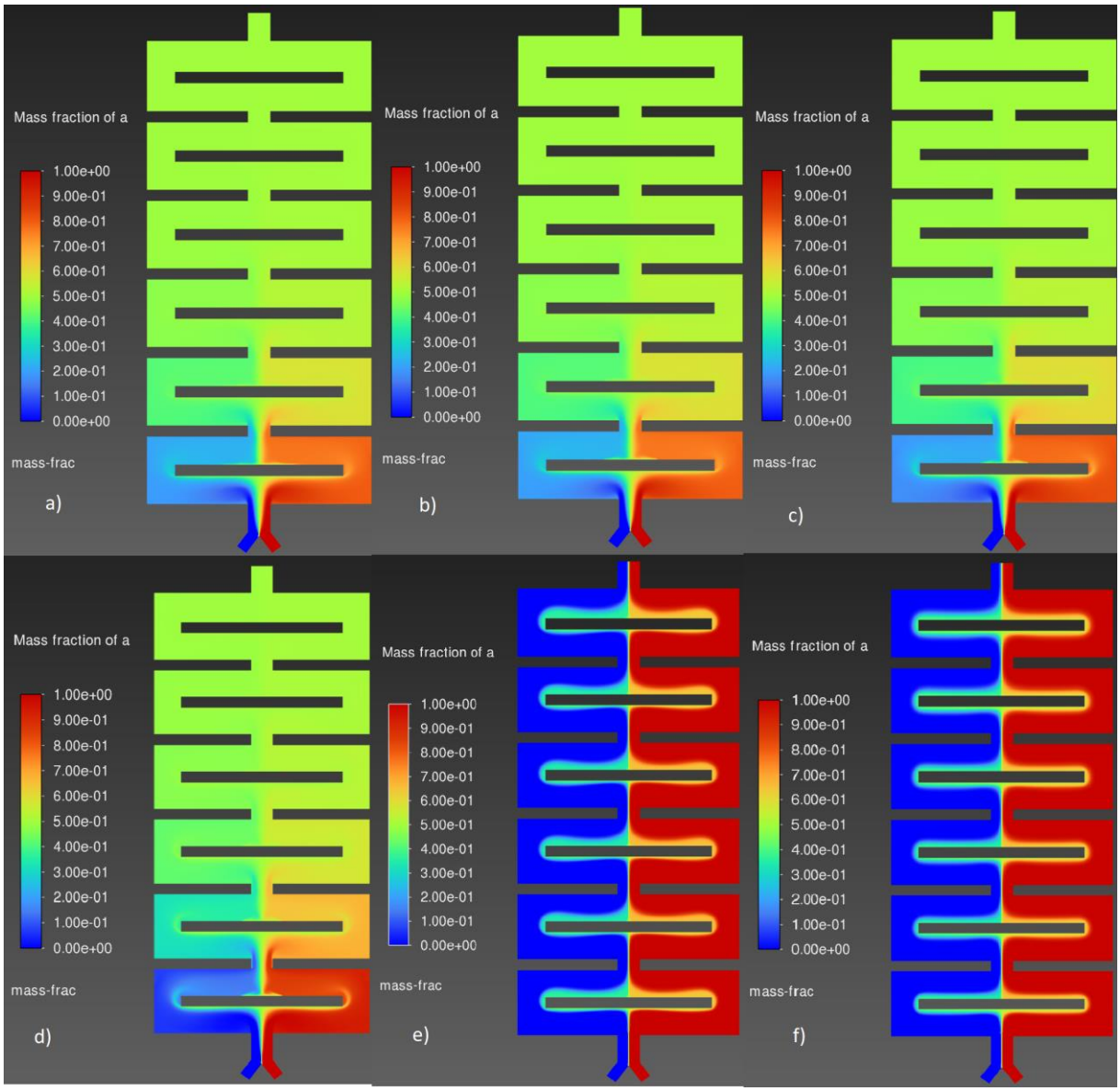

Figure Appendix B-15: Mass fraction contours of species A for different U_{inlet} values: a) 0.25 m·s^{-1}; b) 0.1875 m·s^{-1}; c) 0.125 m·s^{-1}; d) 0.0625 m·s^{-1}; e) 0.0125 m·s^{-1}; f) 0.00125 m·s^{-1}